Simulation of axial tensile well deformation during reservoir compaction in offshore unconsolidated methane hydrate-bearing formation

1. Introduction

Methane hydrate typically exists within the pores of unconsolidated formation under high pressure and low-temperature conditions. As such, methane hydrate is a potential energy resource as it could contain 500 gigatons of carbon [1] equivalent to10 times the amount of world's undiscovered conventional gas resources which are considered to be technically recoverable [2]. Field gas production tests have been conducted in Canada [3], US [4], Japan [5], [6] and China [7], to assess the feasibility of commercial gas production from methane hydrate reservoirs. One of the main challenges toward sustainable gas production has been identified as well/formation integrity due to the unconsolidated nature of the methane hydrate-bearing sediments [8]–[10]. Recent gas production tests at the Nankai Trough in Japan show that sand production issue caused premature termination of the gas production test [6], [11].

Earlier attempts to investigate well integrity in methane hydrate-bearing formation were documented in Freij-Ayoub et al. [12], [13] where they assessed well integrity during heating-induced hydrate dissociation. However, well integrity during reservoir compaction, which might be the cause of the well failure/sand production at the Nankai Trough, was not assessed in their study. Subsequently, well integrity in methane hydrate reservoirs during reservoir compaction was investigated by several researchers ([14], [8], [15] and [9]). Rutqvist et al. [14] showed that the gap between the casing and formation, which developed during well construction (e.g., poor cement job) would adversely affect formation integrity around a horizontal well during gas production. Their work indicates the importance of simulating the well construction processes for the assessment of wellbore integrity during gas production. Qiu et al. [8] simulated 20-day gas production at the Nankai Trough and showed that the casing, cement and screen could accumulate approximately 1% of plastic strain, which they argue would be negligibly small to cause well failure. However, if gas production longer than 20 days were simulated, greater reservoir compaction would occur, and there is a risk of well failure. Yoneda et al. [9] also simulated gas production at the Nankai Trough and found that tensile deformation of the well developed in the overburden layer due to reservoir compaction, which might cause the tensile failure of the gravel pack to induce sand production. This highlights the importance of analyzing the tensile deformation of the well during reservoir compaction. Finally, the work of Shin and Satamarina [15] indicates that well integrity is affected by the change in formation permeability during compaction. If the permeability of the soil is sensitive to porosity reduction during depressurization, then reservoir compaction is inhibited as a low permeability zone develops around the wellbore. This implies that different patterns of permeability change in response to porosity change in the reservoir layer would develop different reservoir compaction profiles, which in turn affects well integrity.

Table 1 shows the list of numerical work on well integrity during reservoir compaction [16], including the ones introduced above. The main shortcomings of these studies are the omission of the well construction process prior to simulating reservoir compaction ([9], [15], [17]–[27]) and omission of the cement sheath ([14], [15], [20]–[24], [28]). Currently, the work by Xu [29] is the only existing work which simulates detailed well construction processes, such as cement shrinkage, and also models the integrity of the cement sheath. In Xu's work, detailed well construction processes including drilling, casing hanging, cementing, cement hardening/shrinkage and casing landing are simulated. After the well construction, well integrity (i.e., casing and cement) during different reservoir compaction profiles were assessed. In the simulation, however, the depressurization (i.e., pore pressure) profile was specified by artificial step functions, and this may have computed unrealistic reservoir compaction profiles. In addition, cement shrinkage values used in the simulation were not representative of the Nankai Trough case, because such cement shrinkage values were not investigated extensively at the time of his work. In addition, the casing-cement interface friction behaviour was not calibrated against experimental data, and the simple Coulomb friction model was employed. In this study, the prior work by Xu [29] is extended by employing (i) depressurization profiles that are physically realistic for hydrate reservoirs; these consist of hydrate dissociated (i.e., high permeability) and undissociated (i.e., low permeability) zones, and also employing (ii) cement shrinkage volume estimated specifically for the Nankai Trough case [30] together with (iii) calibrated casing-cement interface friction model. A parametric numerical study is carried out with an axisymmetric finite element model considering different depressurization and hydrate dissociation profiles in the reservoir.

Table 1 Existing numerical work on well integrity during reservoir compaction expanded from [16].

Authors	Casing	Cement	Formation	Well construction	Reservoir compaction
Bruno & Bovberg (1992)[20]	No	No	Yes	No	Yes
Hamilton et al. (1993)[21]	No	No	Yes	No	Yes
Fredrich et al. (2000)[22]	No	No	Yes	No	Yes
Sayers et al. (2006) [23]	No	No	Yes	No	Yes
Furui et al. (2011)[24]	No	No	Yes	No	Yes
Shin & Santamarina (2016)[15]	Yes	No	Yes	No	Yes
Chia & Bradley (1988)[25]	Yes	Yes	Yes	No	Yes
Yudovich et al. (1988)[27]	Yes	Yes	Yes	No	Yes
Chia & Bradley (1989)[26]	Yes	Yes	Yes	No	Yes
Li et al. (2003)[17]	Yes	Yes	Yes	No	Yes
Li et al. (2005)[18]	Yes	Yes	Yes	No	Yes
Jinnai & Morita (2009)[19]	Yes	Yes	Yes	No	Yes
Yoneda et al. (2018)[9]	Yes	Yes	Yes	No	Yes
Klar et al. (2010)[28]	Yes	No	Yes	Yes	Yes
Rutqvist et al. (2012)[14]	Yes	No	Yes	Yes	Yes
Qiu et al. (2015)[8]	Yes	Yes	Yes	Yes	Yes
Xu (2014)[29]	Yes	Yes	Yes	Yes	Yes

This study focuses on the case of the Nankai Trough methane hydrate-bearing reservoir. Fig**.** 1 shows the location of the Nankai Trough methane hydrate site for the 2013 gas production test [11]. The gas production site was located on the north slope of the Daini Atsumi Knoll off the coast of Japan (Fig. 1a). Three wells were drilled by the drilling vessel D/V Chikyu in 2012: one production well (AT1-P) and two monitoring wells (AT1-MC and AT1-MT1) (Fig. 1b). The methane hydrate reservoir layer is located approximately 300 m below the seafloor, and it has roughly a 50 m thickness. The water depth of the Nankai Trough site is approximately 1,000 m. As the depth of the reservoir layer from the seafloor is relatively shallow, the formation consists of unconsolidated sand and clay. Such formation is susceptible to large volumetric compaction upon depressurization. Therefore, caution must be taken to assess the well integrity in response to reservoir compaction at the Nankai Trough site. Sand production occurred during the six-day gas production test [10], [31], which could be attributed to well failure during the gas production trial.

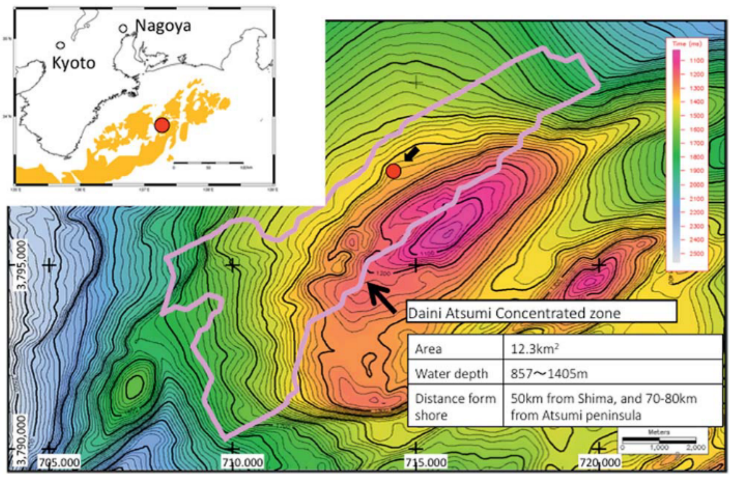

(a)

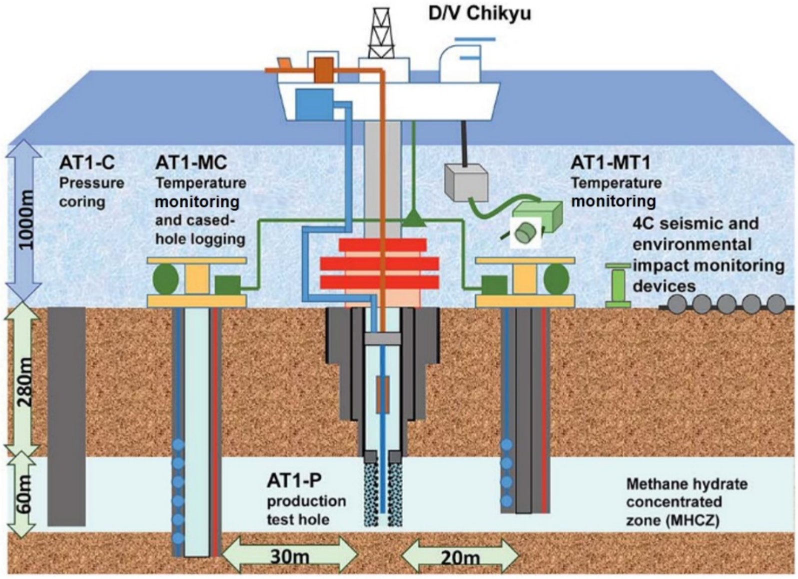

(b)

Fig. 1 Details of the Nankai Trough site for the 2013 gas production test [11]: (a) location of the test site; (b) geometries of the wells and formation layers (courtesy of MH21).

Fig. 2 shows potential well failure mechanisms that may occur at the Nankai Trough site [16]. Uneven hydrate dissociation, which occurs due to heterogeneous hydrate distribution around the well, could cause bending or buckling failure due to the unbalanced lateral support from the reservoir layer. The axial tension failure is caused by the elongation of the overburden formation in response to reservoir compaction, whereas axial compression occurs in the reservoir layer. A deviated well could suffer bending failure at the reservoir layer boundaries. Finally, cement shrinkage could also cause well failure by reducing lateral support for the well.

Among these well failure mechanisms, this paper examines well integrity due to the axial tension mechanism for the following reasons. First, the tensile strength of cement is approximately one-tenth of its compressive strength [32] and thus, the cement is much more likely to fail by tension than by compression. Second, the tension failure could propagate up to the seafloor with the progress of reservoir compaction, whereas the other failure types tend to be localized within the reservoir layer. Therefore, the tension mechanism of well failure is considered to be critical to the long-term sustainable gas production from hydrate reservoirs. As cement shrinkage can affect tensile deformation of the well by reducing the friction at the casing-cement interface, cement shrinkage is considered in this study in combination with reservoir compaction.

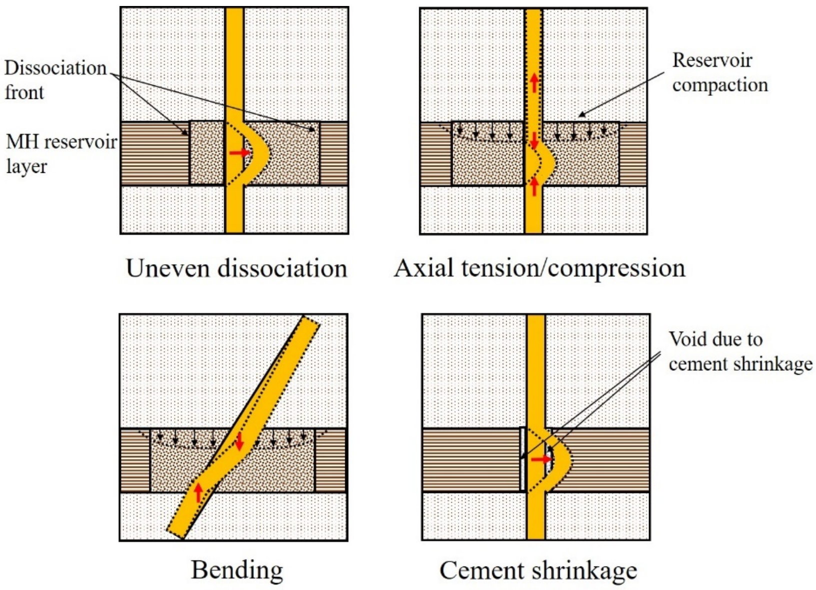

Fig. 2 Failure mechanisms of the well in hydrate reservoirs [16].

Focusing on the Nankai Trough case, the objectives of this study are as follows.

(i) to evaluate the effect of different reservoir compaction patterns on the tensile stress and strain development of the casing/cement in the overburden layer via parametric numerical simulations,

(ii) to evaluate the effect of cement shrinkage volume on tensile deformation of the well in the overburden layer during reservoir compaction, and

(iii) to investigate the correlation between the tensile stress and strain development of the casing/cement in the overburden layer and depressurization/hydrate dissociation patterns in the reservoir.

2. Finite element modelling

2.1. Model geometry

Figure 3 shows a schematic diagram of the axisymmetric finite element model created for this study. The total depth and radius of the model are 650 m and 600 m, respectively. The thickness of the methane hydrate reservoir layer is 50 m, whereas the thicknesses of the overburden and underburden layers are 300 m. A borehole with a radius of 0.312 m (12 1/4 inches) is drilled in the overburden layer. The outer diameter and a wall thickness of the casing placed inside the borehole are 0.122 m (9

5/8 inches) and 0.01 m (0.4 inches), respectively. Cement is placed in the annulus between the casing and formation. The roller boundary constraint is applied at the left and bottom edges of the model whereas a constant distributed pressure load is applied at the top (i.e., hydrostatic pore pressure) and right (i.e., geostatic stress) edges. The top of the model is assumed to be 1,000 m below the sea surface.

Fig. 4 shows the FE mesh of the model. The formation is discretized into 55,250 eight-node displacement four-node pore pressure elements, whereas the casing and cement are discretized into 600 and 1,800 eight-node displacement elements, respectively. The horizontal length of the casing and cement elements is uniformly set to be 5.0×10^{-3} m and 6.3×10^{-3} m, respectively, whereas the horizontal length of the formation elements is increased exponentially with increasing radius from the wellbore (5.3×10^{-2} m at the cement-formation interface and 53 m at the right edge of the model). The vertical length of the mesh is uniformly set to 1 m regardless of the element type.

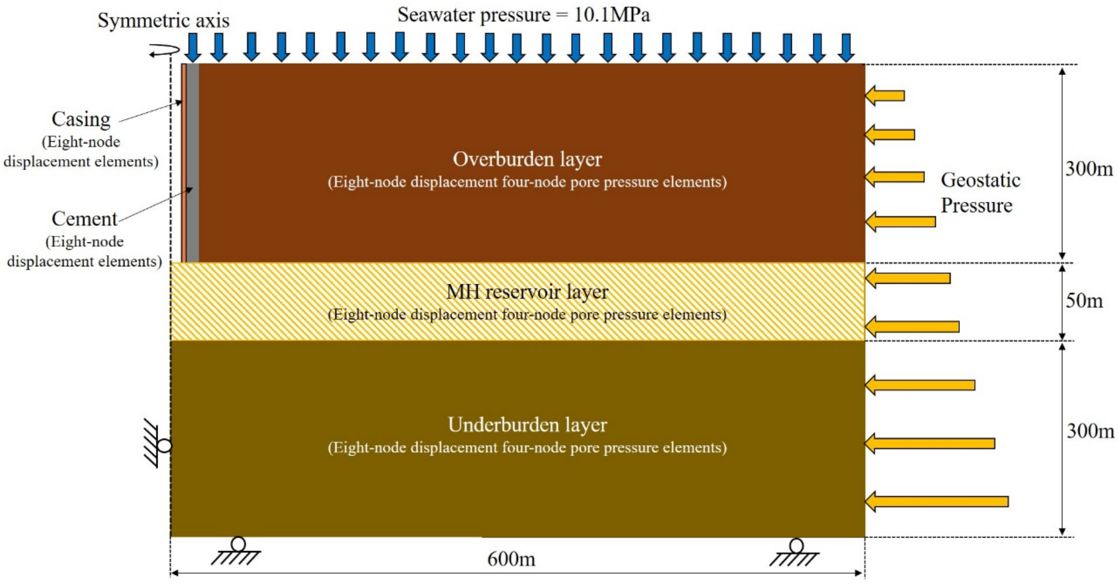

Fig. 3 The geometry of the axisymmetric finite element model.

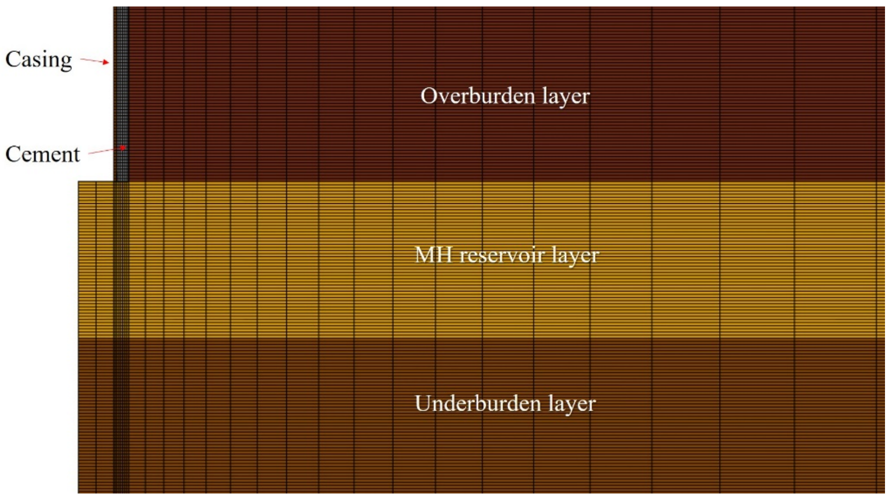

Fig. 4 The mesh of the axisymmetric finite element model near the bottom of the wellbore (enlarged a hundred times in the horizontal direction).

2.2. Simulation steps

2.2.1. Initial conditions

The initial vertical stress distribution of the formation is derived from the *in situ* density measurement data [33]. The initial void ratio distribution is also obtained from the same *in situ* density measurement data. For the initial pore pressure distribution, the hydrostatic pore pressure distribution with the seawater density of 1.027 g/cm^3 is assumed. Two different initial horizontal effective stress profiles (i.e., overconsolidated and normally consolidated overburden cases) are employed, as shown in Fig. 5. The overconsolidated distribution is calculated via Equation 1:

$$\sigma'_h = (1 - \sin\phi')\mathrm{OCR}^{\sin\phi'}\sigma'_v \tag{1}$$

where σ'_h is the horizontal effective stress, σ'_v is the vertical effective stress, ϕ' is the internal friction angle, OCR is the overconsolidation ratio. The OCR values of the overburden layer are derived from triaxial test data on formation core samples retrieved at the Nankai Trough [34], whereas OCR = 1 is employed for the reservoir and underburden layers, in which case Equation 1 reduces to Jaky’s formula. This means that the reservoir and underburden layers are normally consolidated, and this is consistent with the triaxial compression test results on reservoir and underburden sediment cores recovered at the Nankai Trough [9]. Hence, the overconsolidated overburden case is more representative of the actual Nankai Trough formation. For the normally consolidated overburden case, the initial horizontal effective stress is calculated via $\sigma'_h = 0.4\sigma'_v$. The effect of different initial horizontal effective stress distributions is investigated in Section 3.5.

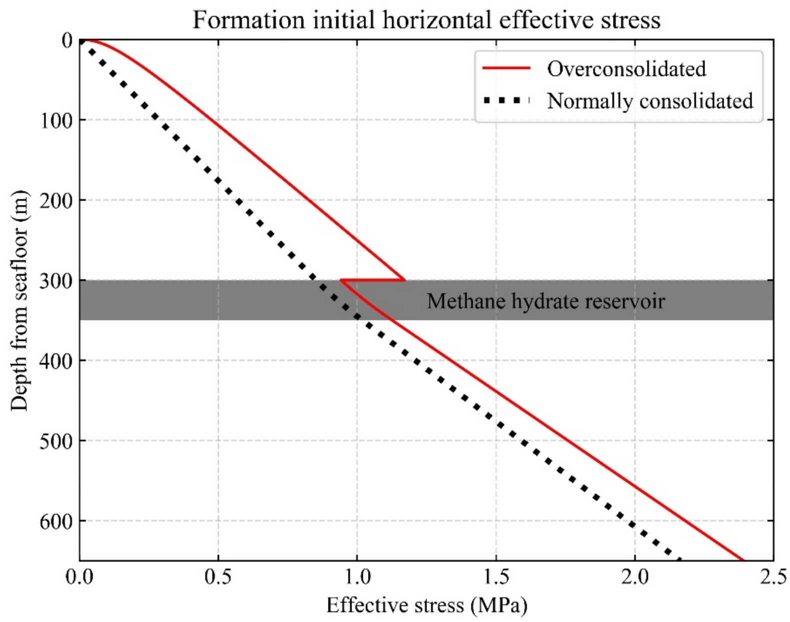

Fig. 5 Initial horizontal effective stress distributions of the formation.

2.2.2. Well construction process

The construction process of the well is incorporated in the simulation. The modelling methodology of the well construction process is identical to the one employed in [35]. The modelled construction stages are listed in Table 2. The cement shrinkage volume of 0.75% is employed in the cement shrinkage stage, which could be expected in the Nankai Trough scenario [30]. The volumetric strain decrement (i.e., volumetric shrinkage) was generated via fictitious thermal contraction by reducing the temperature of the cement elements.

Table 2 The well construction processes incorporated in the simulation.

Construction process	Duration (hour)
1. Drilling	14.4
2. Casing hanging	Immediate
3. Cementing	Immediate
4. Cement hardening/shrinkage	40.8
5. Casing landing	Immediate

2.2.3. Decoupled depressurization and hydrate dissociation process

The depressurization/hydrate dissociation stage is simulated in a decoupled manner by specifying the pore pressure distribution in the reservoir layer, rather than simulating the actual depressurization and dissociation processes in a thermo-hydromechanically coupled manner. This approach allows for creating different reservoir compaction profiles. The analytical steady-state pore pressure distribution shown below is employed to specify the pore pressure distribution in the reservoir layer:

$$u = C_1 \ln\ r + C_2 \tag{2}$$

where u is the pore pressure and r is the radius from the centre of the well. It is assumed that the permeability of the hydrate dissociated zone ($0 \leq r \leq r_f$) is higher than that of the undissociated zone ($r > r_f$). Therefore, the above Equation 2 is applied to each zone separately while satisfying the compatibility of the radial flow velocities at the boundary between the dissociated and undissociated zones. By applying the remaining boundary conditions ($u = P_i$ at $r = r_o$, $u = P_o$ at $r = R_o$), the values of the coefficients (C_1 and C_2) are obtained as follows:

$$C_1 = \begin{cases} (P_o - P_i)/\ln\left(r_f^{1-\alpha_p} R_o^{\alpha_p} / r_o\right) & (0 \le r \le r_f) \\ \alpha_p (P_o - P_i)/\ln\left(r_f^{1-\alpha_p} R_o^{\alpha_p} / r_o\right) & (r > r_f) \end{cases}$$

$$C_2 = \begin{cases} P_i - C_1 \ln r_o & (0 \le r \le r_f) \\ P_o - C_1 \ln R_o & (r > r_f) \end{cases}$$

where P_0 is the hydrostatic pore pressure, P_i is the depressurized pore pressure in the wellbore, r_f is the radius of the hydrate dissociation front, r_o is the radius of the wellbore, R_o is the radius where hydrostatic pore pressure is recovered and α_p is the ratio of the permeability values between the dissociated and undissociated zones. According to the literature, the value of α_p is dependent on the hydrate saturation and it could be ~100 or higher [36]–[38]. In this study, it is set to a constant value of 100. As to the value of r_f, coupled thermo-hydro(mechanical) simulations in the literature [5], [28], [39] suggest that it is a fraction of R_o and increases with larger R_o. In this study, it is assumed that r_f =0.5 R_0.

To model the progress of depressurization and hydrate dissociation, fourteen stages are considered in the simulation. The values of P_i and r_f are linearly varied with time by ΔP_i and Δr_f in each stage from the initial values of $P_i = P_o$ and $r_f = 0$. In the field, the rate of decrease of P_i depends on the speed of depressurization specified by the operator, whereas the rate of increase of r_f depends on the speed of hydrate dissociation, which is governed by the permeability of the reservoir and the heat supply from the far-field. As changes in the formation permeability during hydrate dissociation are complex, the rate of r_f increase may not be constant as assumed in this study. In order to estimate the increase rate of r_f more precisely, it would be necessary to conduct thermo-hydromechanical coupled simulations, similar to the ones presented in the literature [40]–[48].

Fig. 6 shows the simulated pore pressure profiles along the top of the reservoir layer in the case of localized (ΔP_i= -0.3 MPa and Δr_f = 0.5 m) and distributed (ΔP_i = -0.3 MPa and Δr_f = 3 m) hydrate dissociation cases. The former case represents low permeability hydrate-bearing reservoir scenarios, which create a large difference in permeability between the dissociated zone and non-dissociated zone. The latter case represents scenarios of hydrate-bearing formation with high permeability, which results in less variation in permeability between the dissociated zone and non-dissociated zone. To create various depressurization and hydrate dissociation profiles, different combinations of ΔP_i and Δr_f values were employed (i.e., ΔP_i = -0.1, -0.2, -0.3, -0.4, -0.5, -0.6 MPa and Δr_f = 0.5, 1.0, 1.5, 2.0, 2.5, 3.0 m). In total, 36 different depressurization and hydrate dissociation cases were simulated, which are listed in Table 3.

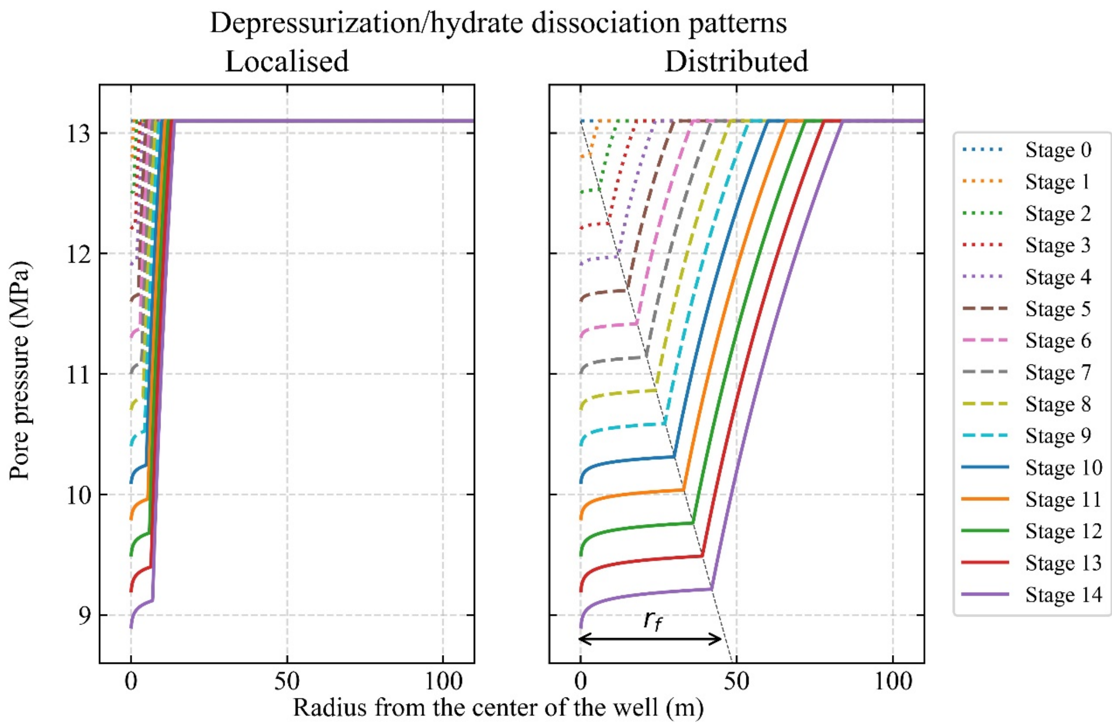

Fig. 6 Simulated depressurization and hydrate dissociation (pore pressure) profiles in the reservoir layer (localized depressurization and dissociation case (ΔP_i = -0.3 MPa and Δr_f = 0.5 m) (left) and distributed depressurization and dissociation case (ΔP_i = -0.3 MPa and Δr_f = 3 m) (right)).

Table 3 The depressurization and hydrate dissociation cases simulated in this study.

Case#	ΔP_i (MPa)	Δr_f (m)	Case#	ΔP_i (MPa)	Δr_f (m)	Case#	ΔP_i (MPa)	Δr_f (m)
1		0.5	13		0.5	25		0.5
2		1.0	14		1.0	26		1.0
3	-0.1	1.5	15	-0.3	1.5	27	-0.5	1.5
4		2.0	16		2.0	28		2.0
5		2.5	17		2.5	29		2.5
6		3.0	18		3.0	30		3.0
7		0.5	19		0.5	31		0.5
8		1.0	20		1.0	32		1.0
9	-0.2	1.5	21	-0.4	1.5	33	-0.6	1.5
10		2.0	22		2.0	34		2.0
11		2.5	23		2.5	35		2.5
12		3.0	24		3.0	36		3.0

2.3. Constitutive models

Soils

The methane hydrate critical state model (MHCS model) [49] is employed to simulate the mechanical behaviour of the soils at the site. The model parameters are calibrated against triaxial test data on formation samples recovered at the Nankai Trough site [50], [51]. Selected calibration results are presented in Fig. 7. Table 4 shows the calibrated values of the MHCS model parameters as well as values of other formation parameters. It is noted that the MHCS parameters (i.e., m_1, m_2, A, B, C, D) in the reservoir layer are set to zero in this study because of the pore pressure fixity in the simulation. This would be a reasonable simplification considering that the hydrate is assumed to have no enhancement effect on the bulk modulus in the MHCS model, i.e., the compaction behaviour of the reservoir layer would not be affected by hydrate saturation. Although it is clear that this assumption of the MHCS model has to be modified to reflect the dependence of bulk compressibility of hydrate-bearing soil on hydrate saturation, this drawback would not generate significant errors in simulating reservoir compaction for the following reasons. First, the majority of reservoir compaction occurs after hydrate-bearing soil undergoes yielding, where hydrate bond between soil particles breaks and the enhancement effect of hydrate is lost. Second, the plastic compression is significantly larger than the preceding elastic compression where the hydrate enhancement effect is still active. Therefore, it is hypothesized in this study that hydrate saturation has negligible effects on the magnitude of reservoir compaction and the simplified approach is taken where the MHCS parameters related to hydrate saturation are all set to zero. This would be a reasonable assumption as compression tests on hydrate-bearing soils revealed that the maximum change in elastic and plastic bulk compressibility were 68% and 73%, respectively, for samples with hydrate saturation ranging between 18% and 85% [52], [53]. This is much smaller than an order of magnitude change, which can be considered negligible in typical soil mechanics terms. The process of dissociation is not considered accordingly; only the process of pore pressure propagation is considered. This simplified approach would simulate scenarios closer to the worst case (the largest possible compaction) for well integrity than the fully-coupled approach, which is convenient from the safety point of view. The values of the density and void ratio of each layer of the formation are chosen based on the *in situ* measurement data at the Nankai Trough [33]; the trend line for the raw density measurements is selected as the density distribution and void ratios are back-calculated by assuming the constant grain density of clay and sand particles (2.65 g/cm^3).

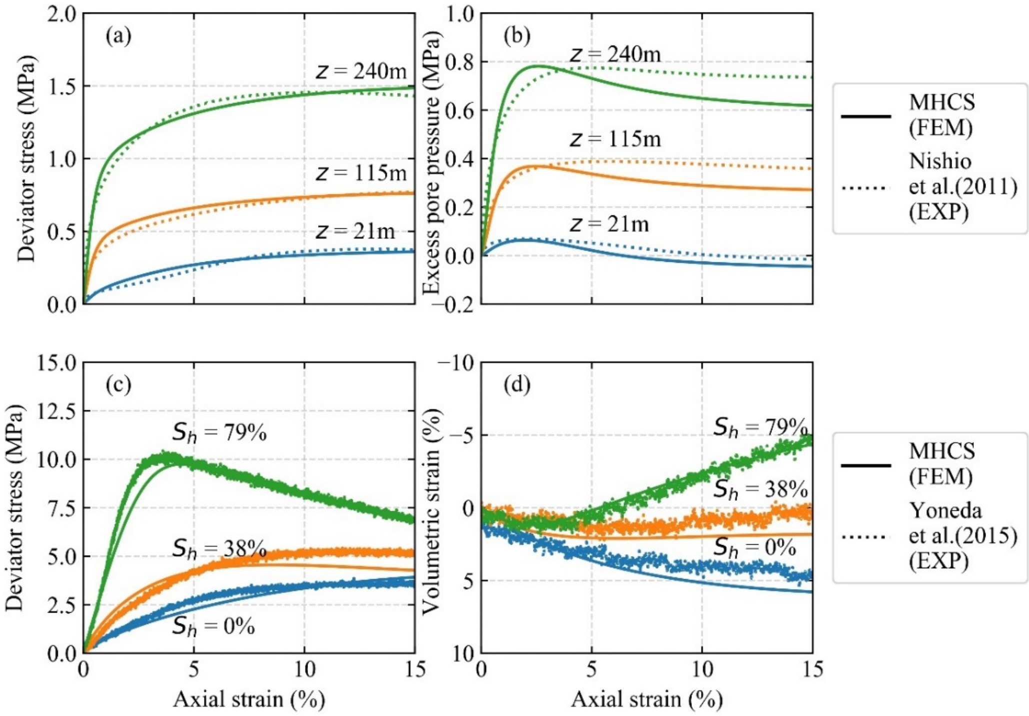

Fig. 7 Calibration result of the MHCS model: (a) deviatoric stress vs. axial strain(clay); (b) excess pore pressure vs. axial strain (clay); (c) deviatoric stress vs. axial strain (sand); (d) volumetric strain vs. axial strain (sand).

Casing and cement

For the casing and cement elements, linear isotropic elasticity with the von Mises yield criteria (casing) and with the Mohr-Coulomb yield criteria (cement) is employed, respectively. The values of the casing and cement constitutive model parameters are listed in Table 5. These values are based on the actual casing and cement employed at the Nankai Trough [8].

Cement-casing and cement-formation interface

The interface behaviour in the contact tangential direction (i.e., interface friction) is modelled by an interface friction constitutive model. The details of the interface friction constitutive model adopted in this study are presented in Appendix A (supplementary material), and its verification is shown in Appendix B (supplementary material). The parameters of the friction model are friction coefficient, cohesion and ultimate elastic interface displacement. Table 6 lists the values of the parameters for the casing-cement and cement-formation interfaces used in the model. The values of the friction coefficient and cohesion for the casing-cement interface are obtained from the literature [54], whereas that of the ultimate elastic interface displacement is calibrated to match the result of a laboratory experiment on a well specimen [55]. Details of the calibration process are provided in Appendix C (supplementary material).

For the cement-formation interface, it is assumed that the interface friction coefficient is identical to that of the underlying formation, and the mean friction coefficient value is calculated from the calibrated values of the critical state frictional constant ($\mu = \tan\left(\sin^{-1}(3\mathrm{M}/(6+\mathrm{M}))\right)$) to be 0.65 and it is used for the entire cement-formation interface. As to the interface cohesion, it is assumed to be negligible as soil particles in the unconsolidated formation would not resist frictional force at zero interface confining pressure (this is experimentally validated in the literature [54]). The value of the ultimate elastic interface displacement is set to 0.25 mm. This is determined by a sensitivity analysis where the reservoir compaction simulation, which is presented in the following sections, is performed with varied values of the ultimate elastic interface displacement between 0.25 mm and 2.5 mm. It was found that results (i.e., the development of stresses and strains in the casing and cement during reservoir compaction) are identical regardless of the different values of the ultimate elastic interface displacement within the examined range. Therefore, the value is set to 0.25 mm in the study. This is supported by an experimental study [56], where the interface shearing between sand and a mortar plate is examined. The study shows that the value of the ultimate elastic interface displacement for the sand-mortar interface is approximately 0.3 mm.

The interface behaviour in the contact normal direction (i.e., interface pressure) is modelled by the ABAQUS inbuilt augmented Lagrange method, which is a combination of the linear penalty method and an augmentation iteration scheme. In the augmented Lagrange method, the contact pressure is calculated by multiplying the stiffness of the representative underlying elements with the interface penetration distance. The interface penetration is maintained below 0.1% of the characteristic element length of the model by iteratively augmenting the contact pressure.

Table 4 The parameter values of the MHCS model for the formation.

	Overburden clay	Methane hydrate reservoir	Underburden sand
Depth from the seafloor (m)	0~300	300~350	350~650
Saturated bulk density (kg/m^3)	1,750	1,750~2,000	2,000
Initial void ratio	1.31	1.31~0.717	0.717
Gradient of compression line, λ	0.18	0.10	0.10
Gradient of swelling line, κ	0.03	0.02	0.02
Critical state frictional constant, M	1.30	1.37	1.37
Poisson's ratio, ν	0.25	0.35	0.35
Subsurface constant, U	15	8	8
Stiffness enhancement constant, m_2	0	0	0
Hydrate degradation constant, m_1	0	0	0

Dilation enhancement constant, *A*	0	0	0
Dilation enhancement constant, *B*	0	0	0
Cohesion enhancement constant, *C*	0	0	0
Cohesion enhancement constant, *D*	0	0	0

Table 5 The parameter values of the constitutive models for the casing (von Mises) and cement (Mohr-Coulomb).

	Casing	Cement
Density (kg/m^3)	7,897	1,198
Young's modulus (GPa)	200	0.131 (slurry) 3.81 (solid)
Poisson's ratio	0.28	0.49 (slurry) 0.20 (solid)
Yield stress (MPa)	379.5	N/A
Friction angle (^{o})	N/A	30
Dilation angle (^{o})	N/A	0
Cohesion (MPa)	N/A	2.72

Table 6 The parameter values of the interface friction constitutive model.

	Casing-cement interface	Cement-formation interface
Friction coefficient (-)	0.8	0.65
Cohesion (MPa)	3.0	0
Ultimate elastic interface displacement (mm)	0.5	0.25

3. Results

3.1. Effect of depressurization/hydrate dissociation patterns

In this section, the effect of depressurization/hydrate dissociation patterns on reservoir subsidence and the stress and strain development of casing and cement is presented. The cement shrinkage volume of

0% and the overconsolidated overburden case are applied.

3.1.1. Formation deformation patterns

Fig. 8 shows the reservoir compaction profiles developed in the two different hydrate dissociation cases. The one on the left-hand side shows the localized dissociation case (Δr_f = 0.5 m), whereas the right-hand side one shows the distributed dissociation case (Δr_f = 3 m). It is noted that the depressurization level is identical between these two cases (ΔP_i = -0.3 MPa), but the pore pressure profiles within the reservoir formation are different, causing different settlement profiles. The values of the maximum subsidence (S_{max}) and the subsidence radius (R_s), which is defined as the radial distance where the curvature of the subsidence distribution becomes maximum, are shown in the figures as circular and square dots, respectively. It is found that the more the hydrate dissociation is localized, the smaller the maximum subsidence and subsidence radius become. The distributed hydrate dissociation case would be analogous to reservoirs in which hydrate dissociation front advances quickly whereas the localized case the slow progress of hydrate dissociation front. The former may be due to high absolute permeability, low hydrate saturation, etc. and the latter the opposite. These two cases are simulated so that a real pore pressure profile during actual depressurization would fall in between these two extreme cases.

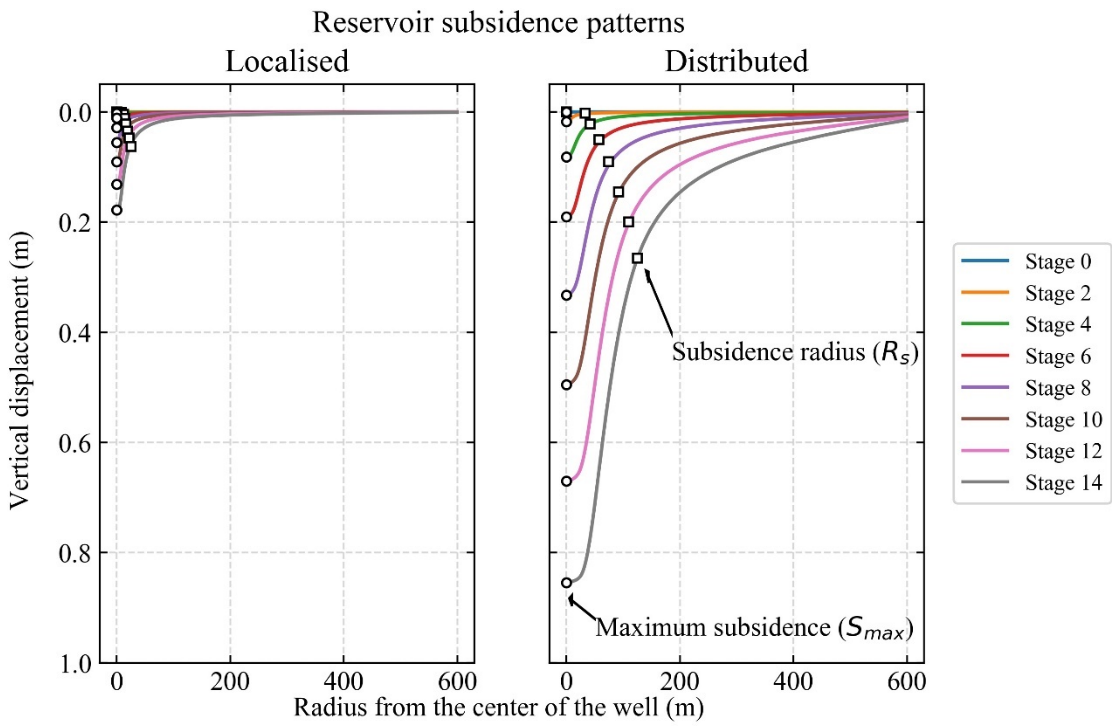

Fig. 8 Reservoir subsidence along the top of the reservoir layer (localized dissociation case (ΔP_i = -0.3 MPa and Δr_f = 0.5 m) (left) and distributed dissociation case (ΔP_i = -0.3 MPa and Δr_f = 3 m) (right)).

Fig. 9 shows the displacement patterns of the reservoir layer at the depressurization stage 14 in the two different hydrate dissociation cases. The magnitudes of the displacement vectors in these figures are normalised and scaled to increase their visibility. The reservoir layer deformation is concentrated near the wellbore in the localised dissociation case, whereas it is more evenly spread radially in the distributed dissociation case.

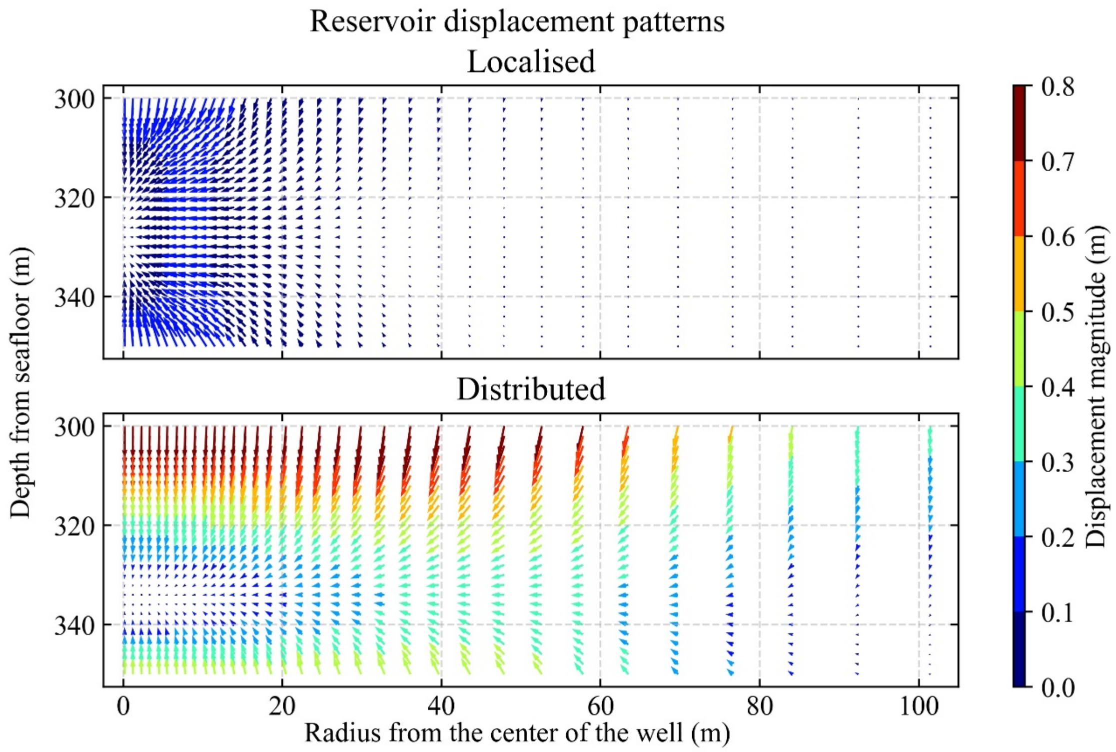

Fig. 9 Deformation patterns of the reservoir layer (localized dissociation case (ΔP_i = -0.3 MPa and Δr_f = 0.5 m) (top) and distributed dissociation case (ΔP_i = -0.3 MPa and Δr_f = 3 m) (bottom)) at the depressurization stage 14. The length of the arrows in each plot is normalized by the maximum magnitude of displacement of respective subsidence cases.

Fig. 10 shows the overburden layer deformation patterns for the two cases. When the reservoir deformation is localised near the wellbore (i.e., localised dissociation case), the overburden layer deformation is localised near the lower centre part. When the reservoir deformation is distributed (i.e., distributed dissociation case), it is more evenly spread in the vertical and horizontal directions. These reservoir/overburden deformation patterns are found to have significant effects on well integrity, which is described in the following sections.

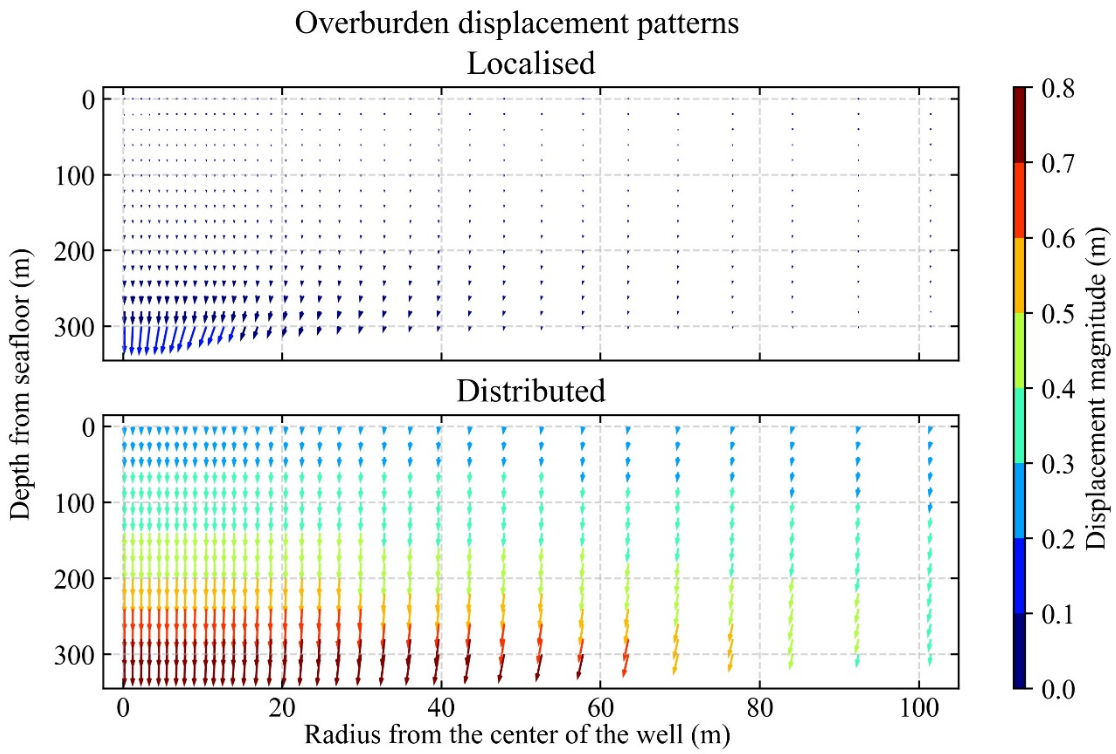

Fig. 10 Deformation patterns of the overburden layer (localized dissociation case (ΔP_i = -0.3 MPa and Δr_f = 0.5 m) (top) and distributed dissociation case (ΔP_i = -0.3 MPa and Δr_f = 3 m) (bottom)) at the depressurization stage 14.

3.1.2. Axial strain and stress development in the casing

Fig. 11 shows the axial strain development along the casing. In both localised and distributed dissociation cases, the maximum axial strain level in the casing is developed near the bottom of the overburden layer (approximately 290 m), and the value is roughly 5,000 με at the dissociation stage 14. However, the average axial strain level along the depth of the casing is greater in the distributed dissociation case than in the localised dissociation case. This corresponds to the overburden layer deformation pattern where the vertical displacement is more evenly spread over the depth of the overburden layer in the distributed dissociation case than in the localised dissociation case. The vertical lines in the figure refer to the yield strain level of the casing material, which indicate the zone of yielding in the casing. The detailed plastic strain profiles are presented in a later section.

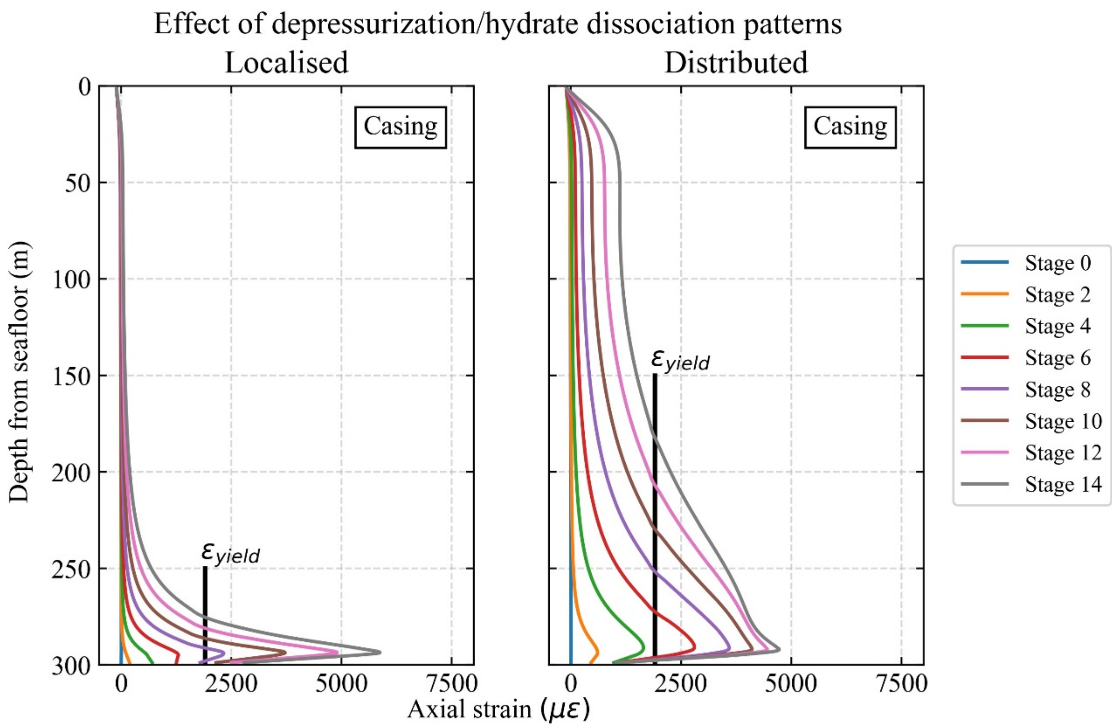

Fig. 11 Axial strain profiles of the casing (localized dissociation case (ΔP_i = -0.3 MPa and Δr_f = 0.5 m) (left) and distributed dissociation case (ΔP_i = -0.3 MPa and Δr_f = 3 m) (right)).

Fig. 12 shows the axial stress development along the casing. The initial axial stress levels of the casing are slightly compressive due to the casing self-weight (i.e., gravitational body force is considered in the simulation) and hydrostatic pressure from the seawater applied at the top of the casing during the well construction process. As is the case in the axial strain development, the maximum axial stress level is developed near the bottom of the overburden layer. The difference is that the axial stress level reaches a plateau once the deviator stress level exceeds the yield stress of the casing (379.5 MPa) and the area of the plateau extends upward with the progress of depressurization/hydrate dissociation stages. The area of axial stress plateau indicates the area of plastic strain development, and it covers the depths between 180 m and 290 m (i.e., 37% of the casing length) at the dissociation stage 14 in the distributed dissociation case. The average axial stress value of the casing is found to be greater in the distributed dissociation case than in the localised dissociation case.

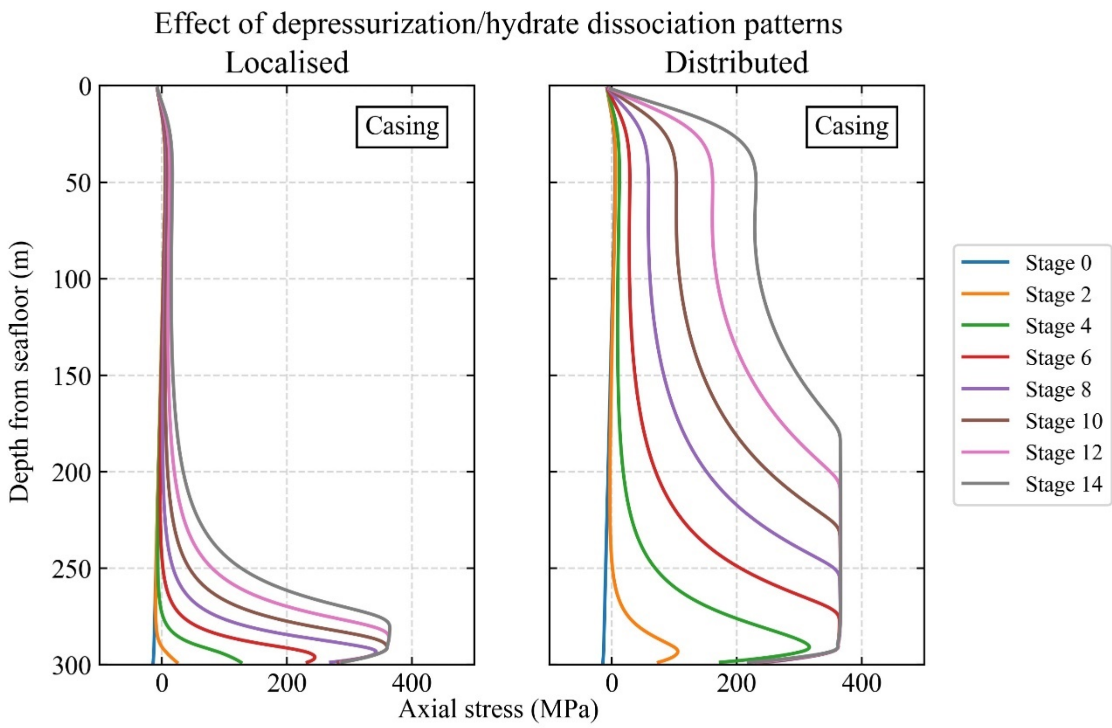

Fig. 12 Axial stress profiles of the casing (localized dissociation case (ΔP_i = -0.3 MPa and Δr_f = 0.5 m) (left) and distributed dissociation case (ΔP_i = -0.3 MPa and Δr_f = 3 m) (right)).

Fig. 13 shows the plastic deviatoric strain development of the casing. The area of the plastic strain development is greater in the distributed dissociation case than in the localised dissociation case, and the area of plastic deviatoric strain development corresponds to the area of the axial stress plateau (i.e., area of yielding) described earlier. The peak value of the plastic deviatoric strain profile is slightly greater in the localised dissociation case at the depressurization stage 14 (4,000 με vs. 2,900 με) because of the localization of casing yielding in the bottom part of the well (270-300 m).

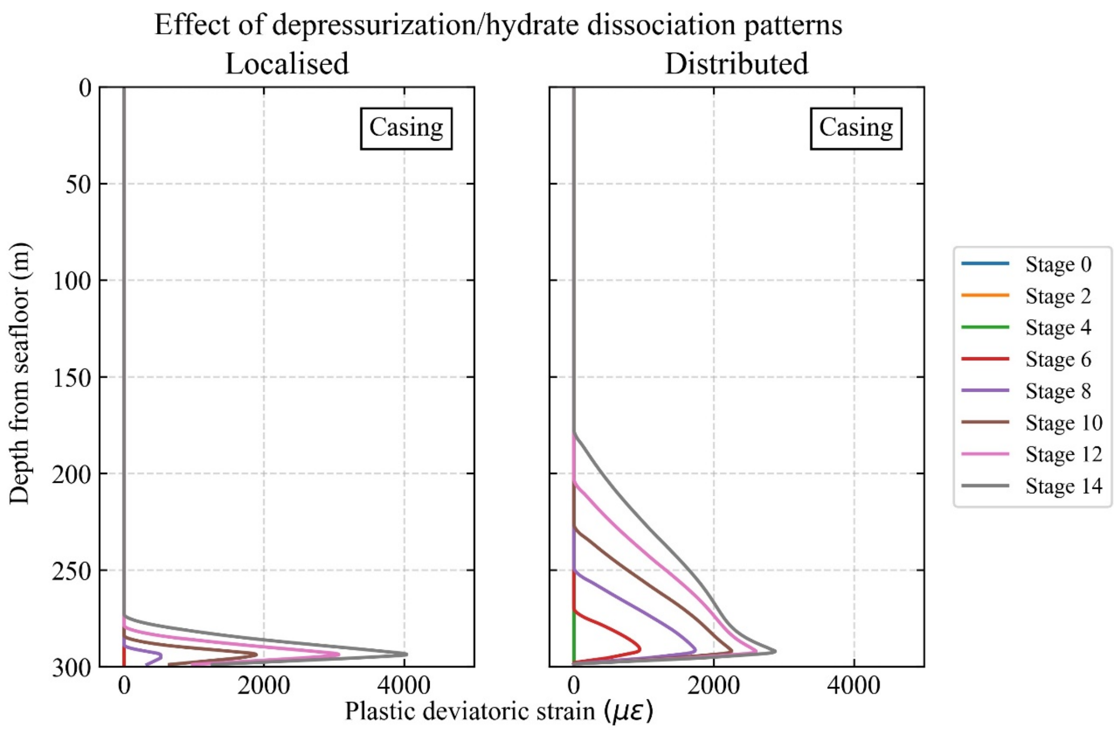

Fig. 13 Plastic deviatoric strain profiles of the casing (localized dissociation case (ΔP_i = -0.3 MPa and Δr_f = 0.5 m) (left) and distributed dissociation case (ΔP_i = -0.3 MPa and Δr_f = 3 m) (right)).

3.1.3. Axial strain and stress development in cement

Fig. 14 shows the axial strain development of the well cement. They are identical to those of the casing, which indicates that the interface slippage at the casing-cement interface is very limited in the simulated reservoir subsidence cases. This also suggests that the axial strain distribution of the casing could be estimated from that of the cement, which can be measured by strain sensors embedded in the cement. Distributed measurement of the axial strain development of the well (with fibre optic sensing techniques, for example) may be applicable for this purpose. An experimental study on the potential of distributed fibre optic monitoring of well integrity is carried out by the authors in a separate study [55]. It is noted that the small compressive strain (i.e., negative strain values) developed at the top of the well is caused during well construction process (casing landing stage), where the casing is released from hanging and compressed in the upper part of the well.

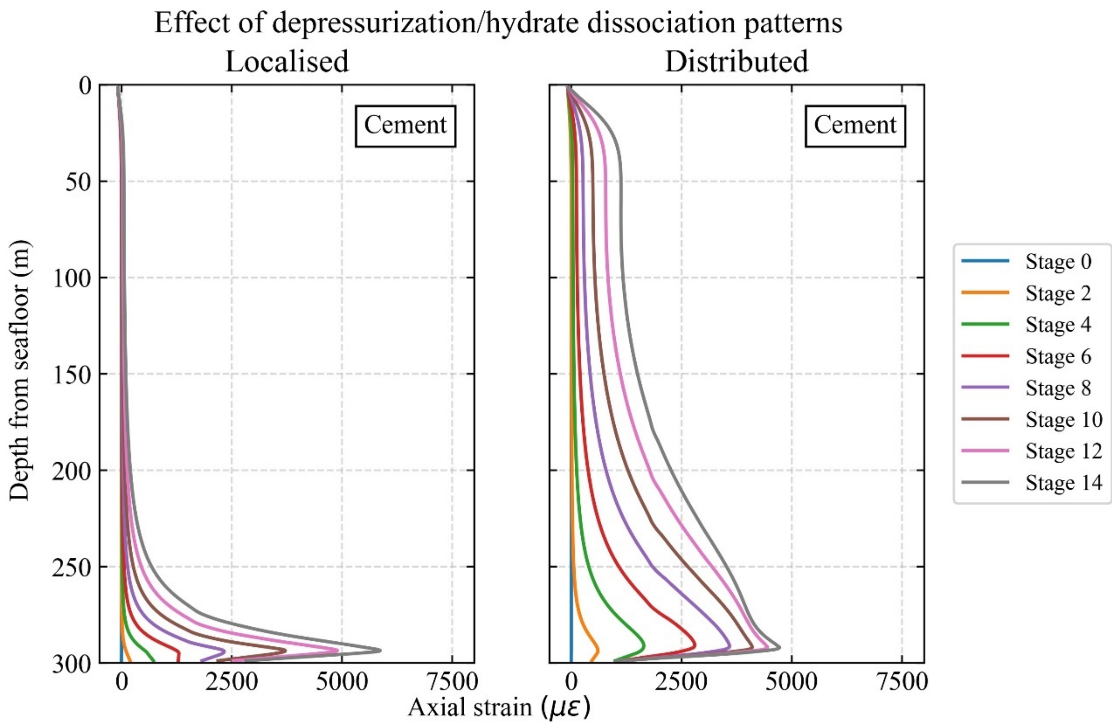

Fig. 14 Axial strain profiles of the cement (localized dissociation case (ΔP_i = -0.3 MPa and Δr_f = 0.5 m) (left) and distributed dissociation case (ΔP_i = -0.3 MPa and Δr_f = 3 m) (right)).

Fig. 15 shows the axial stress development of the cement. The initial axial stress levels of the cement are compressive and change linearly with depths because of the self-weight of the cement and hydrostatic seawater pressure applied at the top of the cement during the well construction process. Due to the smaller stiffness of the cement relative to that of the casing, the axial stress increase (in tension) in the cement is noted to be much smaller than that in the casing. In fact, the axial stress level in the cement does not become tensile (i.e., positive values) throughout the simulated depressurization/hydrate dissociation stages. The axial stress plateau is developed in the cement at the bottom part of the overburden layer as well, while it remains in compression (approximately -2 MPa). This is because the stress state in this area has reached the yield stress state governed by the Mohr-Coulomb criteria, which indicates that the cement fails in shear and not in tension in the simulated depressurization/hydrate dissociation stages. However, if the depth of the well from the sea surface (which is assumed to be 1,000 m in this study) decreases, the initial compressive axial stress levels in the cement also decrease, which in turn could lead to the development of tensile failure prior to the development of shear failure. Hence, the initial stress state corresponding to the depth of the well from the sea surface would be an important factor in assessing the cement integrity.

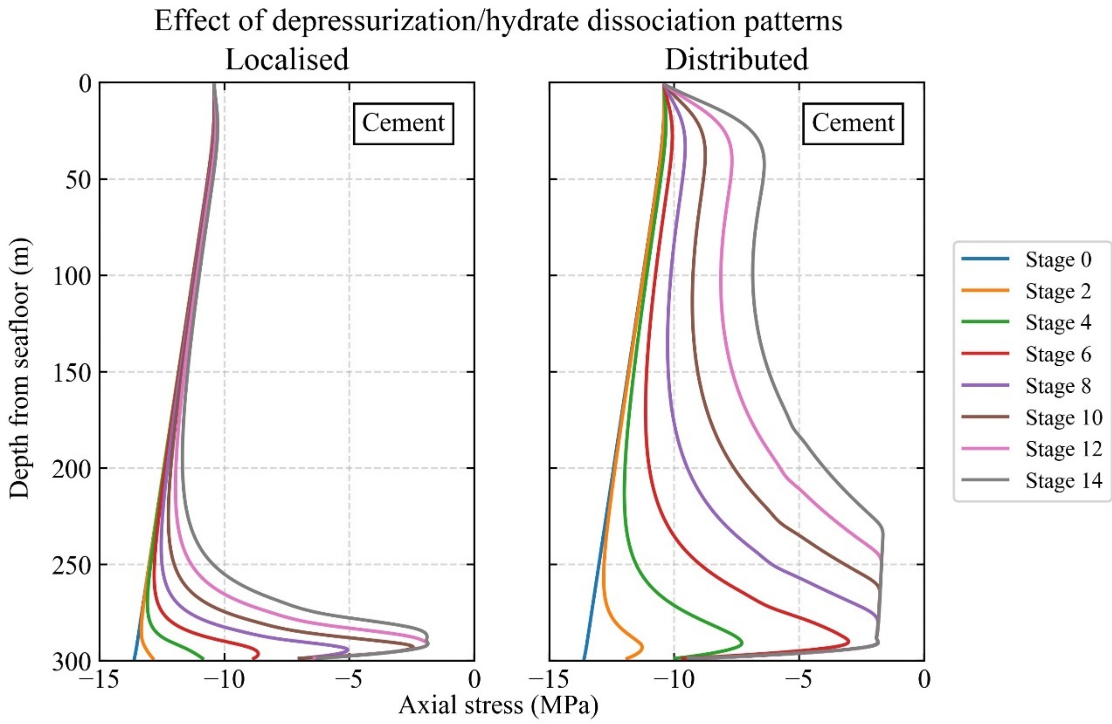

Fig. 15 Axial stress profiles of the cement (localized dissociation case (ΔP_i = -0.3 MPa and Δr_f = 0.5 m) (left) and distributed dissociation case (ΔP_i = -0.3 MPa and Δr_f = 3 m) (right)).

Fig. 16 shows the plastic strain profiles in the cement, which are qualitatively similar to the ones for the casing shown earlier. The difference is that the peak value of the plastic deviatoric strain at the depressurization stage 14 is much greater in the cement than that in the casing (2,900 με (casing) vs. 7,400 με (cement) in the distributed dissociation case and 4,000 με (casing) vs. 13,000 με (cement) in the localised dissociation case). This is because the area of yielding in the cement is localised within a smaller area than that in the casing, which reflects the brittleness of the shear failure of the cement.

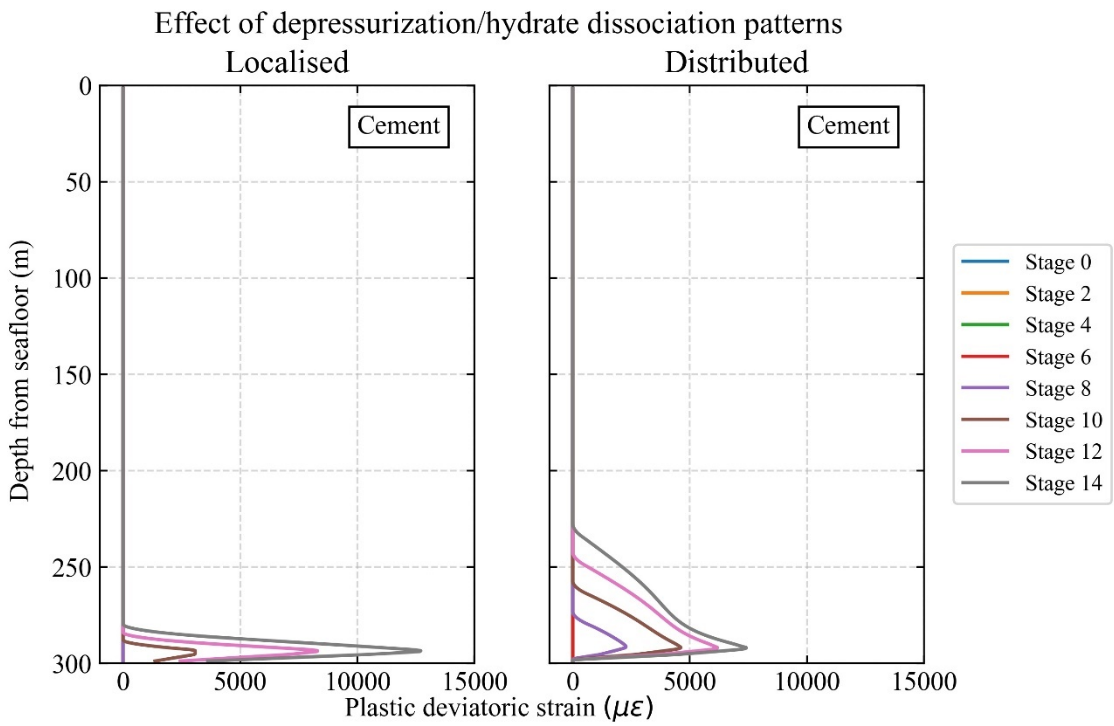

Fig. 16 Plastic deviatoric strain profiles of the cement (localized dissociation case (ΔP_i = -0.3 MPa and Δr_f = 0.5 m) (left) and distributed dissociation case (ΔP_i = -0.3 MPa and Δr_f = 3 m) (right)).

3.2. Effect of cement shrinkage

Cement shrinkage occurs due to the capillary pressure development in the cement pores during the cement hydration process. In the Nankai Trough formation case, the cement shrinkage volume could potentially reach 0.75% [30]. Therefore, in this study, the volume of the cement elements is decreased by 0.75% in the cement shrinkage stage to assess its effect on well integrity.

Fig. 17 shows the axial stress development of the cement with the cement shrinkage volume of 0% and 0.75%. The initial axial stress levels of the cement in the 0.75% shrinkage case are significantly larger (less compressive) than in the 0% shrinkage case. This is because cement shrinkage during the well construction process is simulated under the zero axial displacement condition (i.e., radial cement shrinkage), which results in the decrease of the initial compressive axial stress generated by cement self-weight and hydrostatic seawater pressure. It is noted that the axial stress levels do not become tensile; instead, they reach limiting compressive stress values specified by the Mohr-Coulomb yield surface.

In the subsequent depressurization stages, the cement is stretched in the axial direction due to reservoir compaction, causing the reduction in the initial compressive axial stress levels. In the 0% shrinkage case, the stress plateau (i.e., Mohr-Coulomb yield surface) is reached in the depressurization stage 8, whereas the cement has already yielded in the depressurization stage 0 in the 0.75% shrinkage case as mentioned earlier, and the axial stress level in the cement remains constant at approximately -2 MPa throughout the subsequent depressurization stages. The negative residual axial stress values show that the plastic deformation of the cement in the 0.75% shrinkage case occurs in shear but not in tension, as is the case for the 0% shrinkage scenario.

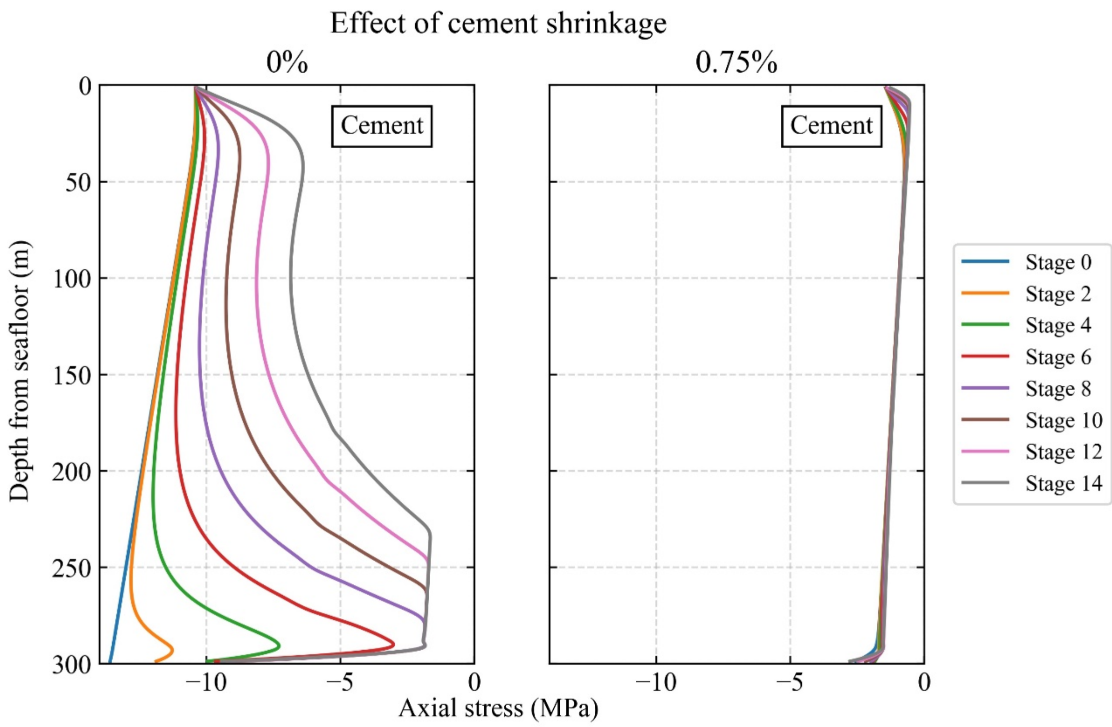

Fig. 17 Axial stress profiles of the cement with the cement shrinkage volume of 0% and 0.75% (ΔP_i = -0.3 MPa and Δr_f = 3 m).

Fig. 18 shows the plastic deviatoric strain development of the cement. The average plastic strain level of approximately 6,600 με is already developed in the cement due to the cement shrinkage volume of 0.75%, and it increases with the progress of reservoir subsidence to the maximum value of 24,000 με at the subsidence stage 14 at the bottom part of the well. This maximum plastic deviatoric strain value is three times greater than that in the 0% cement shrinkage case (7,400 με vs. 24,000 με).

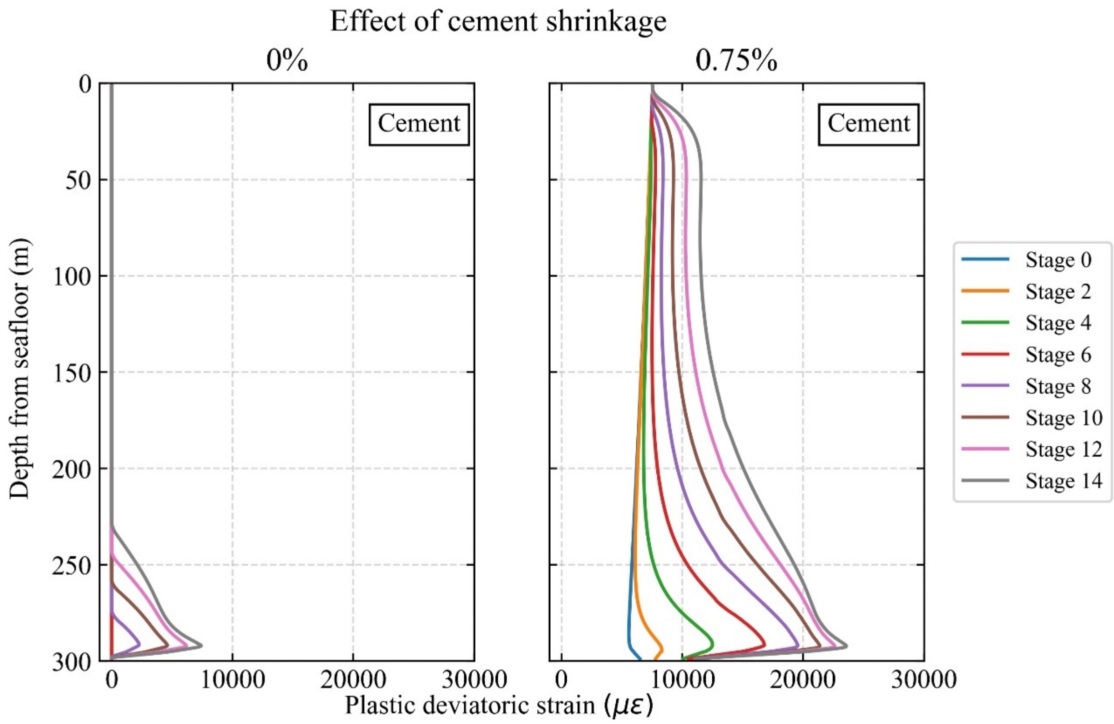

Fig. 18 Plastic deviatoric strain profiles of the cement with the cement shrinkage volume of 0% and 0.75% (ΔP_i = -0.3 MPa and Δr_f = 3 m).

Fig. 19 shows the axial strain development of the casing and cement with the cement shrinkage volume of 0% and 0.75%. It is found that, unlike the axial stress development, the axial strain development of the cement is not affected by the cement shrinkage. Also, the axial strain profiles of the casing and cement are found to be identical to each other. These results suggest that the interface slippage is not induced at either the formation-cement or cement-casing interface by the cement shrinkage volume of 0.75%.

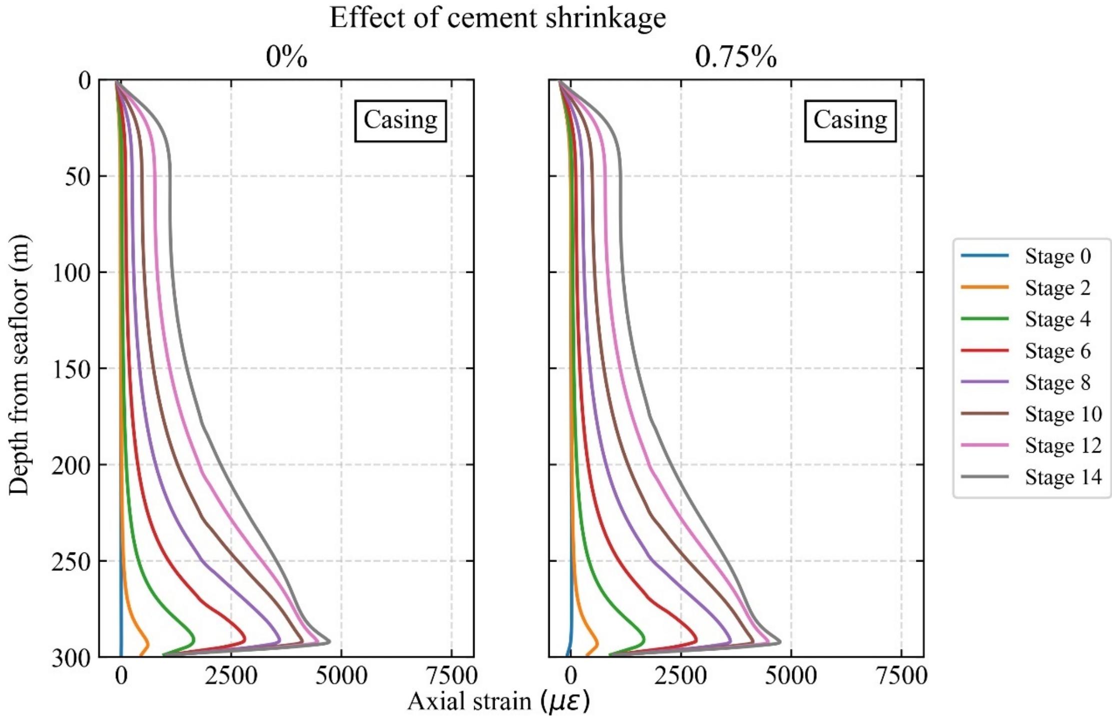

(a)

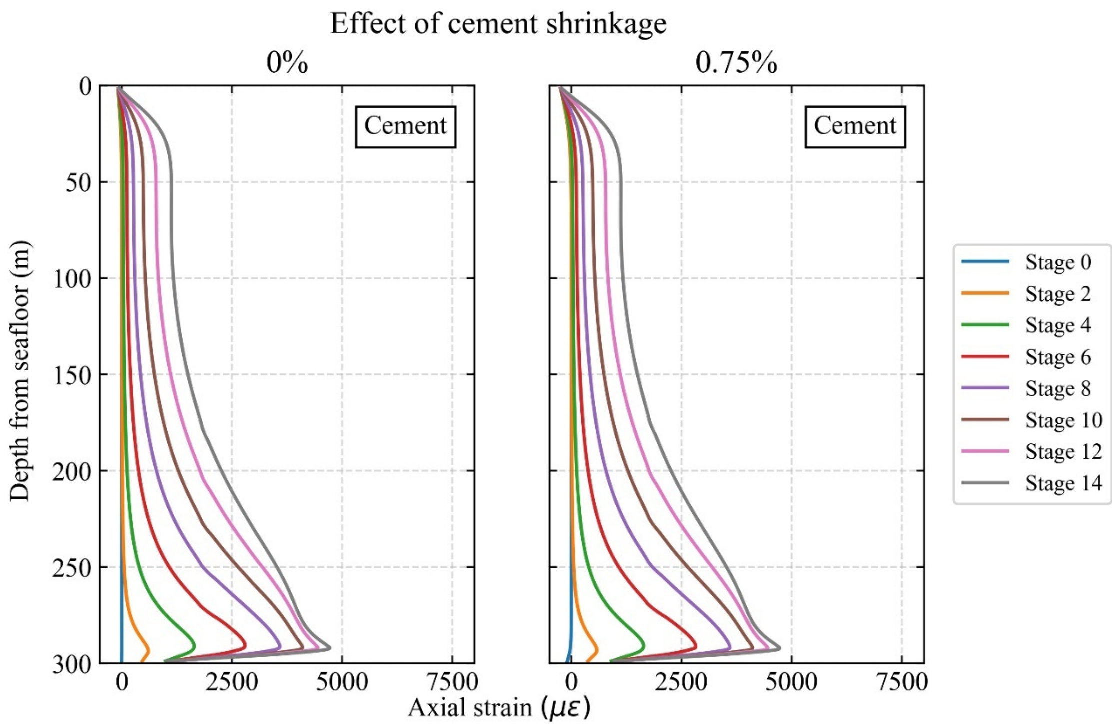

(b)

Fig. 19 Axial strain profiles of (a) the casing and (b) the cement with the cement shrinkage volume of

0% and 0.75% (ΔP_i = -0.3 MPa and Δr_f = 3 m).

A back-of-the-envelope calculation is performed with the analytical solution for the cavity expansion/contraction of an elastic cylinder. The decrease in the radial effective stress at the cement-formation interface due to cement shrinkage can be calculated by Equation 3:

$$\Delta\sigma'_r = G\left(\left(\frac{r_c}{r_o}\right)^2 - 1\right)\frac{\Delta V_{cement}}{100} \tag{3}$$

where $\Delta\sigma'_r$ is the change in the radial effective stress, G is the shear modulus of the formation, r_c is the outer radius of the casing, r_o is the radius of the wellbore and ΔV_{cement} is the volume shrinkage of the cement in percent. Equation 3 is valid for small shrinkage volume ($\Delta V_{cement} \ll 100\%$). The value of shear modulus of the overburden layer at 200 m below the seafloor is approximately 40 MPa and the value of r_c/r_o is 0.7857. By setting the value of ΔV_{cement} to 0.75%, the decrease in the radial effective stress is calculated to be $\Delta\sigma'_r$ = -0.115 MPa. The corresponding decrease in the ultimate interface shear stress at the cement-formation interface is $\Delta\tau_{ult} = \mu\Delta\sigma'_r =$ -0.092 MPa (μ = 0.8). This decrease in the interface shear resistance is too small to initiate interface slippage. The above discussion is relevant to the cement-formation interface. As to the casing-cement interface, the interface pressure increases (rather than decreases) due to cement shrinkage, which reduces the potential of interface slippage. This is because the cement shrinkage induces inward radial displacement, where the cement tries to separate from the formation but at the same time press against the casing wall. Therefore, the cement shrinkage volume of 0.75% does not affect the shaft friction development at the cement-formation or casing-cement interface, and hence the axial strain development of the casing and cement is not altered by the 0.75% cement shrinkage either.

3.3. Effect of the initial horizontal stress of the formation

The simulation results presented in the earlier sections are computed with an assumption that the overburden clay layer is overconsolidated, which would be reasonable according to the triaxial test results on formation samples recovered at the Nankai Trough [34]. However, the actual stress state of the Nankai Trough formation contains uncertainty due to the fact that the site is located in the subduction zone where the geologic conditions are complex. Also, the formation samples examined in the triaxial tests were found to be significantly disturbed during sampling, which decreases the reliability of the estimation. Therefore, additional simulations for the normally consolidated overburden case are conducted. The reservoir and underburden layers are assumed to be normally consolidated regardless of the simulation cases. The difference in the horizontal stress profiles between the consolidated and normally consolidated overburden cases are shown earlier in Fig. 5. It is noted that the cement shrinkage volume was set to 0% for both cases.

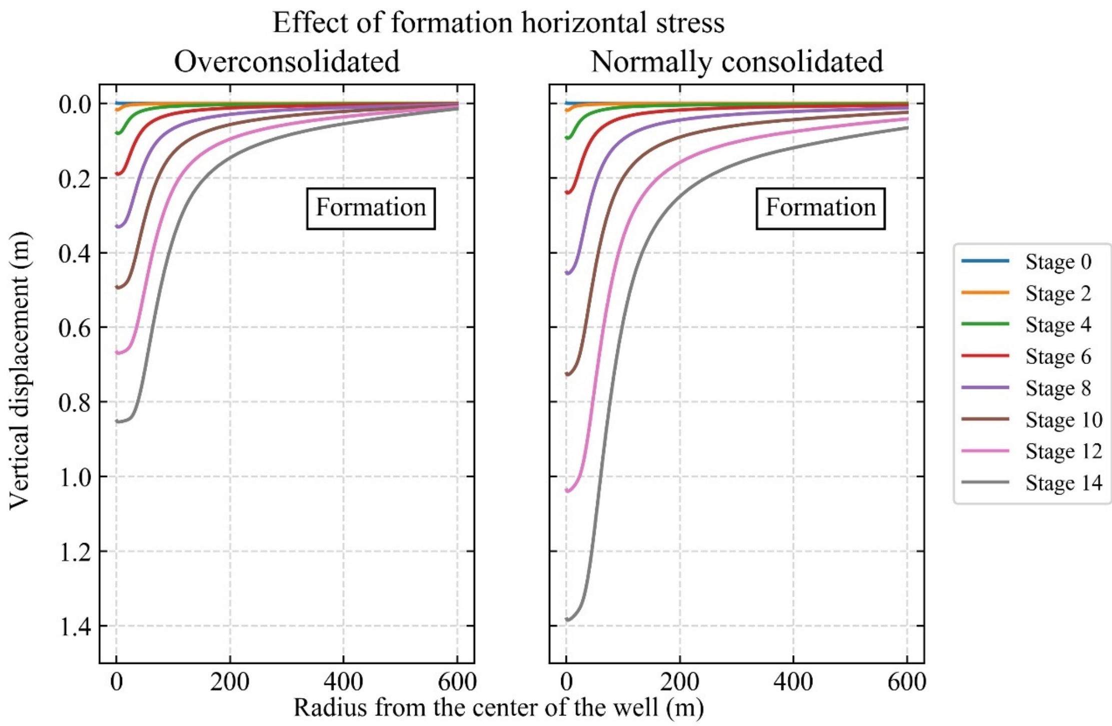

Fig. 20 Reservoir subsidence along the top of the reservoir layer in the overconsolidated and normally consolidated cases (ΔP_i = -0.3 MPa and Δr_f = 3 m).

Fig. 20 shows the reservoir subsidence profiles for the overconsolidated and normally consolidated overburden cases. The maximum reservoir subsidence at the depressurization/hydrate dissociation stage 14 increases from 0.85 m (overconsolidated case) to 1.4 m (normally consolidated case). This is because the ratio of vertical effective stress to horizontal effective stress (i.e., K_0 value) becomes smaller in the normally consolidated overburden case (0.40) relative to the overconsolidated case (0.44), which results in greater magnitudes of volumetric plastic strain (relative to plastic deviatoric strain) computed in the MHCS model.

Because the reservoir subsidence increases in the normally consolidated overburden case compared to the overconsolidated overburden case, the axial and plastic deviatoric strain development of the casing and cement also become greater. Fig. 21 shows the axial strain development of the casing and cement. The maximum axial strain level in the casing increases from approximately 4,700 με (overconsolidated overburden case) to 7,100 με (normally consolidated overburden case), and so does the maximum axial strain level in the cement. However, the axial strain profiles of the casing and cement are still identical in both overconsolidated and normally consolidated overburden cases, indicating that the change in the radial effective stress between the overconsolidated and normally consolidated overburden cases (K_0 value change from 0.44 to 0.40) does not induce interface slippage at the casing-cement interface. Fig. 22 shows the plastic deviatoric strain development of the casing and cement. It is found that the maximum plastic deviatoric strain levels in the casing and cement (at stage 14) increase from 2,900 με (casing) and 7,400 με (cement) (overconsolidated overburden case) to 5,300 με (casing) and 18,000 με (cement) (normally consolidated overburden case), respectively. The area where the casing and cement develop plastic strain increase significantly for the normal consolidated overburden case as well. Therefore, the initial horizontal stress levels of the formation have significant effects on well integrity during reservoir compaction.

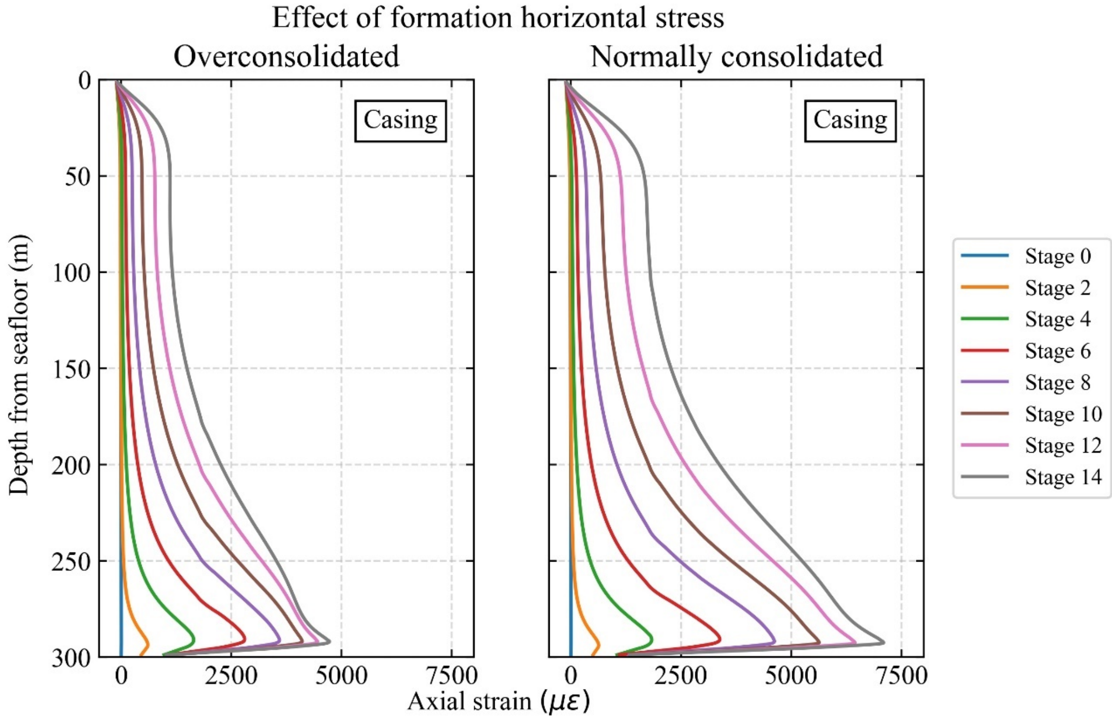

(a)

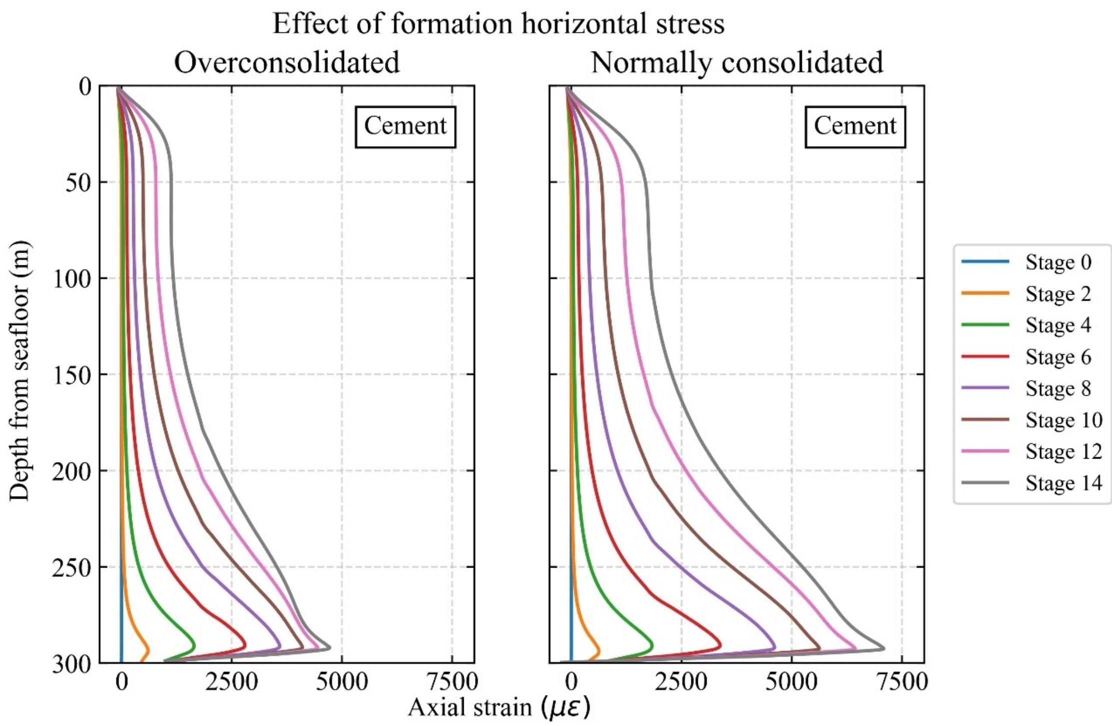

(b)

Fig. 21 Axial strain profiles of (a) the casing and (b) the cement in the overconsolidated and normally consolidated cases (ΔP_i = -0.3 MPa and Δr_f = 3 m).

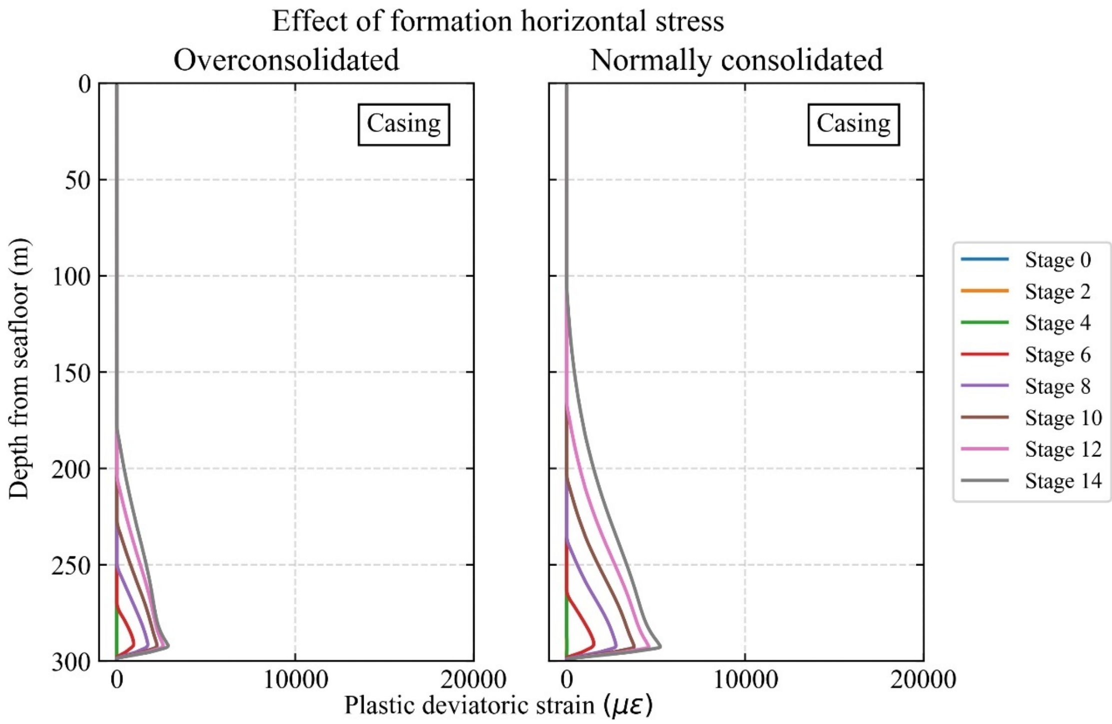

(a)

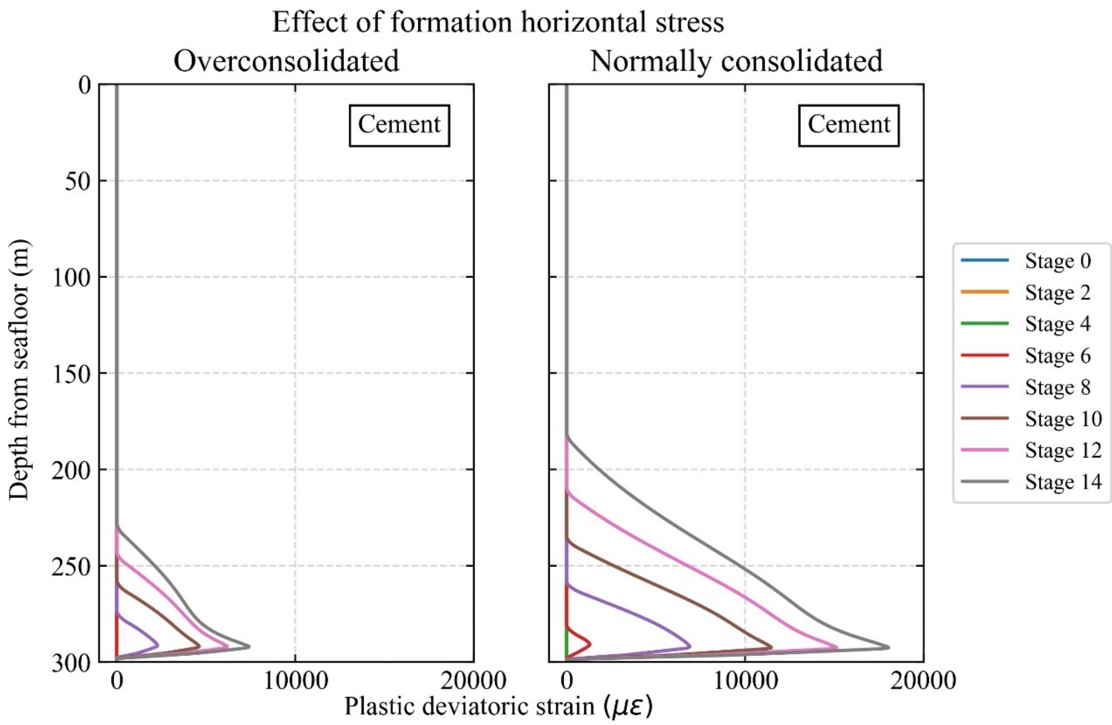

(b)

Fig. 22 Plastic deviatoric strain profiles of (a) the casing and (b) the cement in the overconsolidated and normally consolidated cases (ΔP_i = -0.3 MPa and Δr_f = 3 m).

4. Discussion

The results shown in the previous section indicate that the pattern of depressurization/hydrate dissociation scenarios (i.e., localized and distributed dissociation cases) influences the distributions of stresses and strains in the casing and cement. Fig. 23 shows a schematic diagram summarizing how different hydrate dissociation patterns (at the same pressure drawdown) result in different reservoir subsidence profiles. In general, the localized dissociation case induces smaller values of maximum reservoir subsidence and subsidence radius than the distributed dissociation case. This is because when the radius of hydrate dissociation front (r_f) is small, pressure drawdown does not propagate afar in the reservoir in the radial direction, resulting in smaller reservoir volume subjected to compaction.

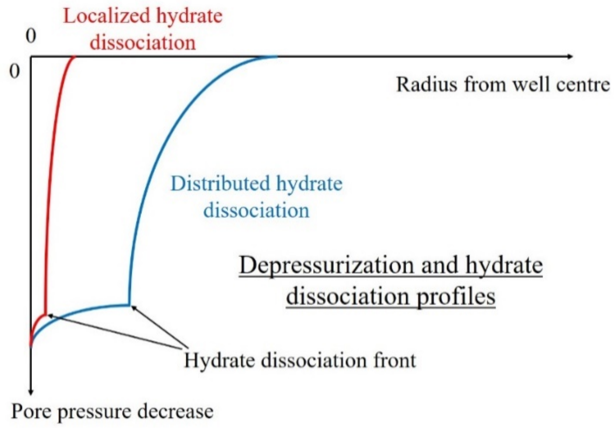

(a)

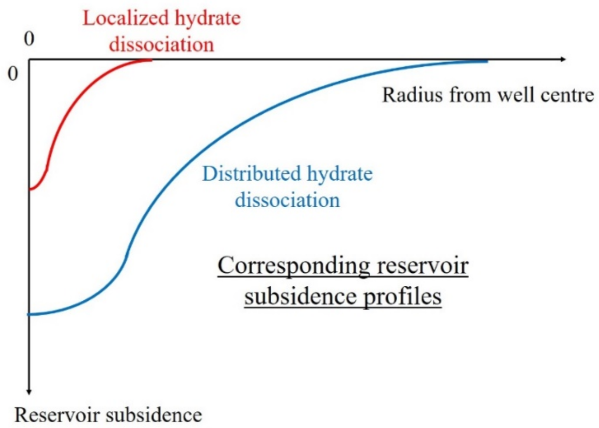

(b)

Fig. 23 Effect of different depressurization/hydrate dissociation patterns on reservoir subsidence characteristics: (a) input pore pressure profiles; (b) output reservoir subsidence profiles.

In this section, contour plots are created to evaluate the maximum axial and plastic deviatoric strains as well as the plasticity length developed in the casing and cement at different values of pressure drawdown ($\sum \Delta P_i$) and radius of hydrate dissociation front ($\sum \Delta r_f$).

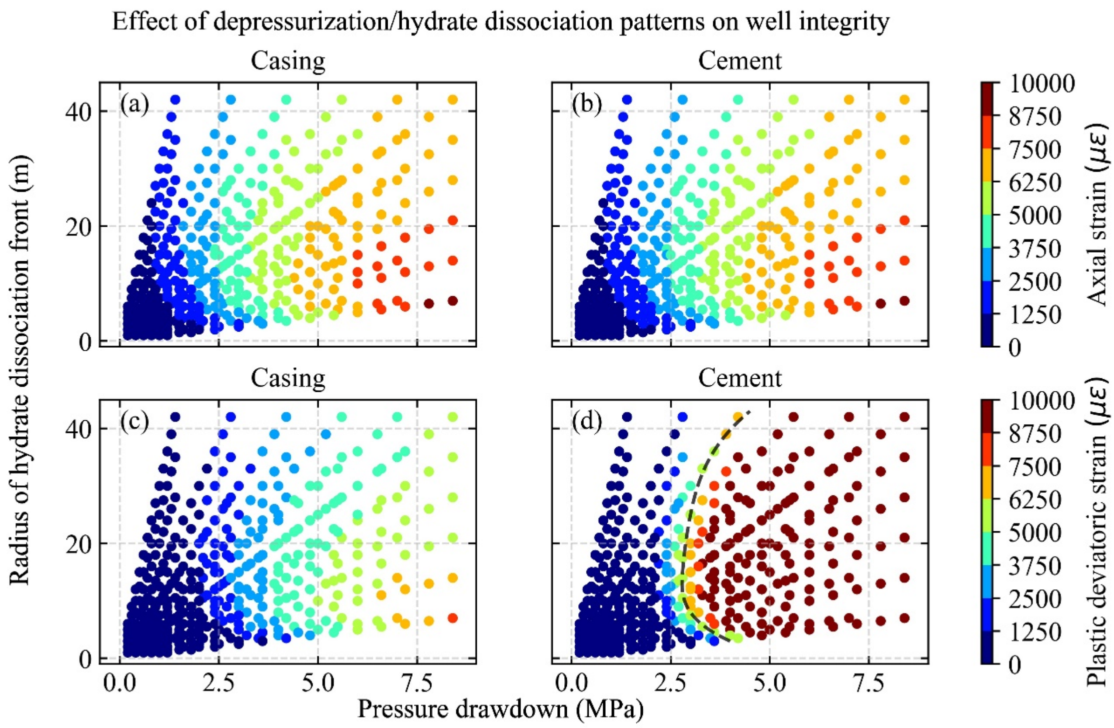

Fig. 24 The effect of depressurization/hydrate dissociation patterns on well integrity: (a) casing axial strain; (b) cement axial strain; (c) casing plastic deviatoric strain; (d) cement plastic deviatoric strain.

Fig. 24 shows the change in the maximum axial and plastic deviatoric strain levels in the casing and cement subjected to different depressurization/hydrate dissociation patterns. A data point on the contour plot is extracted from each of the fourteen depressurization/hydrate dissociation stages in each of the thirty-six simulation cases (i.e., 504 data points in total). Results show that the larger the pressure drawdown and the smaller the radius of hydrate dissociation front are, the greater the maximum axial strain levels in the casing and cement become (Fig. 24a and b). For example, when the radius of hydrate dissociation front is only 5 m as the pressure drawdown of 8 MPa is maintained, the maximum axial strain levels in the casing and cement could both reach 10,000 με (i.e., 1%). This level of strain does not cause failure in the casing, which is ductile enough to withstand up to several tens of percent strain, but potentially not in the cement which is a much more brittle material than the casing. Fig. 24c and d show the maximum plastic deviatoric strain levels in the casing and cement. Plastic deviatoric strain levels change gradually in the casing with the change of pressure drawdown and radius of hydrae dissociation. On the other hand, large values of plastic deviatoric strain develop rapidly in the cement when the pressure drawdown and radius of hydrate dissociation front exceed the values along the dashed line shown in Fig. 24d. Hence, the plastic strain level increases significantly. This indicates that the cement failure could be highly localized in the form of a shear band.

These results suggest that, in order to avoid the development of large axial strain levels in the casing and cement, the pressure drawdown may have to be kept at a low level until the radius of hydrate dissociation front increases above a certain value. For instance, when the axial strain level of 10,000 $\mu\varepsilon$ needs to be avoided, the pressure drawdown would have to be temporarily held at 6 MPa until the radius of hydrate dissociation front reaches 25 m.

It is noted that the simulated pressure drawdown and the radius of hydrate dissociation front are assumed to increase simultaneously and linearly with time in this study. This may not be realistic considering that it is usual to perform a rapid pressure drawdown in the field practice, which would not cause a noticeable increase in the radius of hydrate dissociation front. The pressure drawdown will be maintained while the radius of hydrate dissociation front increases to produce gas from the hydrate reservoir. Hence, the effect of the path of pressure drawdown and changes in the radius of hydrate dissociation front has to be investigated extensively considering the stress/strain development of the well.

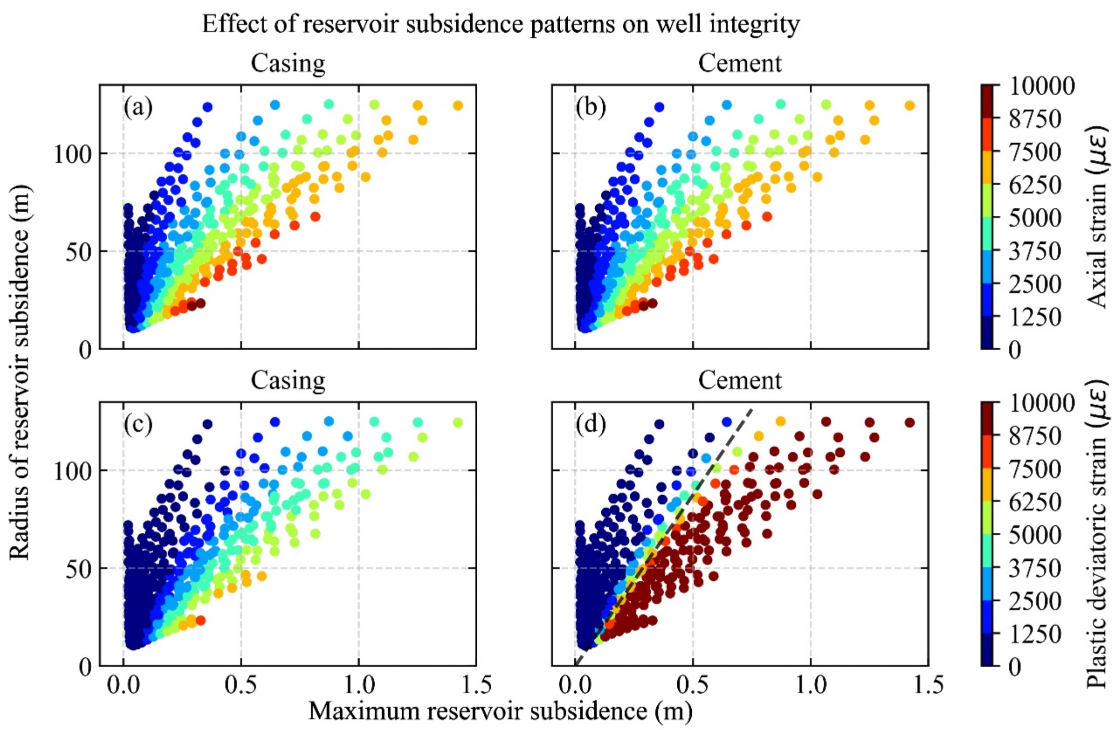

Fig. 25 The effect of reservoir subsidence characteristics on well integrity: (a) casing axial strain; (b) cement axial strain; (c) casing plastic deviatoric strain; (d) cement plastic deviatoric strain.

Fig. 25 shows the change in the maximum axial and plastic deviatoric strain levels in the casing and cement with changing reservoir subsidence characteristics. The results show that the larger the maximum reservoir subsidence and the smaller the subsidence radius are (i.e., the more the reservoir compaction is localised), the greater the maximum axial strain levels in the casing and cement become (Fig. 25a and b). As to the plastic strain development, the maximum plastic deviatoric strain level in the casing changes gradually with changes in the reservoir subsidence characteristics. On the other hand, large plastic deviatoric strain levels develop abruptly in the cement. In this study, the two distinct areas of the damaged (below the line) and undamaged (above the line) cement are identified in Fig. 25d. The line of separation can be approximated by Equation 4:

$$R_s = 175\ S_{max} \qquad (4)$$

where R_s is the radius of formation subsidence and S_{max} is the maximum formation subsidence.

Although the proposed line separates the damaged and undamaged cement areas clearly, the position and shape of the line could be affected by the initial hydrate distribution in the reservoir, which is highly heterogeneous in the field. In this study, the effect of hydrate saturation on reservoir compaction is not considered (i.e., hydrate saturation values in the reservoir are uniformly set to zero). This assumption may be acceptable because it is assumed in the soil model that hydrate saturation has negligible effects on the compressibility of the hydrate-bearing soil. However, the shear resistance will be enhanced by the presence of hydrate, which helps the reservoir resist inward displacement during depressurization/hydrate dissociation through the cavity contraction mechanism. Therefore, the effect of hydrate saturation on the characteristics of reservoir subsidence can be examined in a future study by conducting a fully coupled thermo-hydromechanical simulation that computes deformations in the reservoir with complex hydrate saturation profiles. Also, a sensitivity analysis of the MHCS model parameters may be conducted to investigate their effect on the risk plots. This will allow incorporating the uncertainty of parameter values as they were determined through trial-and-error curve fitting against laboratory experiment data on formation samples without proper optimization.

5. Conclusions

In this study, a parametric study of well integrity under different reservoir subsidence patterns for the case of the Nankai Trough methane hydrate reservoir is carried out by conducting a series of finite element simulations. The well construction processes are incorporated prior to the reservoir subsidence stages to investigate the effect of cement shrinkage on well integrity during reservoir compaction. Also, the effect of the initial horizontal stress profile of the formation (i.e., overconsolidated and normally consolidated overburden cases) on well integrity is assessed. The model parameters for the simulations (soil, cement, casing and the interfaces) are calibrated against relevant laboratory test data. The primary findings of this study are presented below:

(i) Various reservoir subsidence profiles are simulated for the Nankai Trough case to examine the scenarios when the maximum reservoir subsidence and the radius of formation subsidence vary between 0.01 m and 1.42 m, and 10.5 m and 125 m, respectively. These subsidence profiles correspond to the pressure drawdown of between 0.1 MPa and 8 MPa, and hydrate dissociation front radius of between 0.5 m and 42 m. The largest maximum axial strain levels developed in the casing and cement are both 9,500 $\mu\varepsilon$, and the largest plastic deviatoric strain levels are 7,700 $\mu\varepsilon$ (casing) and 29,000 $\mu\varepsilon$ (cement). With these levels of strains, the casing would still be far from failure (which would require ~30% strain), and the plasticity gradually spread in a region with depths of approximately 100 m to 300m. On the other hand, localised failures such as shear band may develop in the cement.

(ii) A large pressure drawdown combined with a small radius of hydrate dissociation front, which corresponds to higher ratios of reservoir subsidence to the lateral extent of subsidence, is found to induce the largest levels of axial and plastic deviatoric strain in the casing and cement. Therefore, such a ratio could be used to predict cement damage (e.g., cement could be damaged if the ratio exceeds 175). These results indicate that the well integrity would be the most vulnerable in the initial stages of hydrate dissociation after rapid depressurization. In order to prevent well failure, the pressure drawdown may need to be kept at a low level (e.g., several MPa) until hydrate dissociation front advances to a certain radius (e.g., a couple of tens of metres).

(iii) The effect of cement shrinkage during wellbore construction on wellbore stability was examined for the two scenarios. Cement shrinkage volume of 0.75% is found to develop approximately 6,600 με plastic deviatoric strain in the cement prior to reservoir subsidence, and it increases to the maximum value of 24,000 με by the time reservoir subsidence reaches 0.85 m. Compared to the 0% shrinkage case, the maximum plastic deviatoric strain increases by more than 200% (7,400 με vs. 24,000 με) due to the cement shrinkage of 0.75%. The effect of initial in-situ horizontal stress on wellbore stability was also examined. The slight decrease in the initial horizontal stress levels of the formation (K_0 = 0.44 vs. 0.40) was found to increase the maximum plastic deviatoric strain level in the cement by more than 100%. Results suggest that the underestimation of cement shrinkage and overestimation of formation horizontal stress could have contributed to well failure at the Nankai Trough site.

The developed well integrity contour plots, as shown in Fig. 24 and Fig. 25, will be useful for evaluating the risk of casing and cement damage during gas production from methane hydrate reservoirs, provided that either hydrate dissociation front or maximum reservoir subsidence and subsidence radius data are available. Coupled thermo-hydromechanical simulations of hydrate dissociation-induced reservoir compaction will not only provide such data (which are difficult to obtain through field measurements) but could also be used to update the risk plots. It can incorporate the effect of highly heterogeneous distributions of hydrate saturation on the development of pore pressure (depressurization) and subsidence profiles in the reservoir layer during gas production. Therefore, coupled thermo-hydromechanical simulations for the well integrity analysis needs to be conducted in future studies.

Acknowledgements

The funding for a part of this research has been provided by the MH21 Research Consortium in the Ministry of Economy, Trade and Industry (METI) via Japan Oil, Gas and Metals National Corporation (JOGMEC). The authors would like to express sincere gratitude for their financial support. The authors worked for the Geomechanics modelling and monitoring studies under the MH21 program funded by the Japanese Ministry of Trade, Economy and Industry [16]. This study is motivated by the past work and discussion with the MH21 team.

References

[1] M. Maslin, M. Owen, R. Betts, S. Day, T. Dunkley Jones, and A. Ridgwell, "Gas hydrates: past and future geohazard?," *Philos. Trans. R. Soc. A Math. Phys. Eng. Sci.*, vol. 368, pp. 2369–2393,

2010, doi: 10.1098/rsta.2010.0065.

[2] U.S. Geological Survey, “An Estimate of Undiscovered Conventional Oil and Gas Resources of the World, 2012,” pp. 1–5, 2012.

[3] K. Yamamoto and S. R. Dallimore, “Aurora-JOGMEC-NRCan Mallik 2006-2008 gas hydrate research project progress,” *Fire Ice*, vol. Summer, pp. 1–5, 2008, [Online]. Available: https://www.netl.doe.gov/research/oil-and-gas/methane-hydrates/fire-in-the-ice.

[4] H. Farrell *et al.*, “Iġnik Sikumi gas hydrate field trial completed,” *Fire in the Ice*, vol. 12(1), pp. 1–3, 2012.

[5] L. Chen, Y. Feng, T. Kogawa, J. Okajima, A. Komiya, and S. Maruyama, “Construction and simulation of reservoir scale layered model for production and utilization of methane hydrate: The case of Nankai Trough Japan,” *Energy*, vol. 143, pp. 128–140, 2018, doi: 10.1016/j.energy.2017.10.108.

[6] K. Yamamoto *et al.*, “Operational overview of the first offshore production test of methane hydrates in the Eastern Nankai Trough,” in *Proceedings of the Offshore Technology Conference*, 2014, pp. 1–11, doi: 10.4043/25243-MS.

[7] L. Chen, Y. Feng, J. Okajima, A. Komiya, and S. Maruyama, “Production behavior and numerical analysis for 2017 methane hydrate extraction test of Shenhu, South China Sea,” *J. Nat. Gas Sci. Eng.*, vol. 53, pp. 55–66, 2018, doi: 10.1016/j.jngse.2018.02.029.

[8] K. Qiu, K. Yamamoto, R. Birchwood, and Y. Chen, “Well Integrity Evaluation for Methane

Hydrate Production in the Deepwater Nankai Trough," *SPE Drill. Complet.*, vol. 30, no. 1, pp. 52–67, 2015, [Online]. Available: https://doi.org/10.2118/174081-PA.

[9] J. Yoneda *et al.*, "Mechanical Response of Reservoir and Well Completion of the First Offshore Methane-Hydrate Production Test at the Eastern Nankai Trough: A Coupled Thermo-Hydromechanical Analysis," *SPE J.*, vol. 24, no. 02, pp. 531–546, 2018, doi: 10.2118/191145-PA.

[10] S. Uchida, A. Klar, and K. Yamamoto, "Sand production model in gas hydrate-bearing sediments," *Int. J. Rock Mech. Min. Sci.*, vol. 86, pp. 303–316, 2016, doi: 10.1016/j.ijrmms.2016.04.009.

[11] K. Yamamoto *et al.*, "Thermal responses of a gas hydrate-bearing sediment to a depressurization operation," *RSC Adv.*, vol. 7, no. 10, pp. 5554–5577, 2017, doi: 10.1039/C6RA26487E.

[12] R. Freij-Ayoub, B. Clennell, B. Tohidi, J. Yang, and R. Hutcheon, "Casing integrity in hydrate bearing sediments," in *Proceedings of the 6th International Offshore Site Investigation and Geotechnics Conference*, 2007, pp. 103–112, [Online]. Available: https://www.onepetro.org/download/conference-paper/ARMA-09-138?id=conference-paper%2FARMA-09-138.

[13] R. Freij-Ayoub, C. Tan, B. Clennell, B. Tohidi, and J. Yang, "A wellbore stability model for hydrate bearing sediments," *J. Pet. Sci. Eng.*, vol. 57, pp. 209–220, 2007, doi: 10.1016/j.petrol.2005.10.011.

[14] J. Rutqvist, G. J. Moridis, T. Grover, S. Silpngarmlert, T. S. Collett, and S. A. Holdich, “Coupled multiphase fluid flow and wellbore stability analysis associated with gas production from oceanic hydrate-bearing sediments,” *J. Pet. Sci. Eng.*, vol. 92–93, pp. 65–81, 2012, doi: 10.1016/j.petrol.2012.06.004.

[15] H. Shin and J. C. Santamarina, “Sediment-well interaction during depressurization,” *Acta Geotech.*, vol. 12, no. 4, pp. 883–895, 2016, doi: 10.1007/s11440-016-0493-1.

[16] T. Sasaki, “Fibre optic monitoring and finite element analysis of well integrity in methane hydrate reservoirs,” PhD thesis. University of Cambridge, 2019.

[17] X. Li, F. L. Mitchum, M. Bruno, P. D. Pattillo, and S. M. Willson, “Compaction, Subsidence, and Associated Casing Damage and Well Failure Assessment for the Gulf of Mexico Shelf Matagorda Island 623 Field,” in *Proceedings of the SPE Annual Technical Conference and Exhibition*, 2003, pp. 1–15, doi: 10.2118/84553-ms.

[18] X. Li, S. J. Tinker, M. Bruno, and S. M. Willson, “Compaction Considerations for the Gulf of Mexico Deepwater King West Field Completion Design,” in *Proceedings of the SPE/IADC Drilling Conference*, 2005, pp. 1–14, doi: 10.2118/92652-MS.

[19] Y. Jinnai and N. Morita, “Analysis of Casing-Shift Problems in Compacting Reservoirs,” *SPE Drill. Complet.*, vol. 24, no. 02, pp. 332–345, 2009, doi: 10.2118/111243-pa.

[20] M. S. Bruno and C. A. Bovberg, “Reservoir compaction and surface subsidence above the Lost Hills Field, California.,” *Int. J. Rock Mech. Min. Sci. Geomech. Abstr.*, vol. 30, no. 2, p. A136,

1992, [Online]. Available: https://doi.org/10.1016/0148-9062(93)91213-3.

[21] J. M. Hamilton, A. V. Maller, and M. D. Prins, "Subsidence-Induced Shear Failures Above Oil and Gas Reservoirs," *Int. J. Rock Mech. Min. Sci. Geomech. Abstr.*, vol. 30, no. 2, p. A136, 1993, doi: ISBN 90 5410 0451.

[22] J. T. Fredrich, J. G. Arguello, G. L. Deitrick, and E. P. Rouffignac, "Geomechanical Modeling of Reservoir Compaction, Surface Subsidence, and Casing Damage at the Belridge Diatomite Field," *SPE Reserv. Eval. Eng.*, vol. 3, no. 4, pp. 8–10, 2000, doi: 10.2118/65354-PA.

[23] C. M. Sayers, L. Den Boer, D. W. Lee, P. J. Hooyman, and R. P. Lawrence, "Predicting Reservoir Compaction and Casing Deformation in Deepwater Turbidites using a 3D Mechanical Earth Model," in *Proceedings of the First International Oil Conference and Exhibition*, 2006, pp. 1–7, doi: 10.2118/103926-MS.

[24] K. Furui, G.-F. Fuh, and N. Morita, "Casing and Screen Failure Analysis in Highly Compacting Sandstone Fields," in *Proceedings of the SPE Annual Technical Conference and Exhibition*, 2011, pp. 1–17, doi: 10.2118/146231-MS.

[25] Y. P. Chia and D. A. Bradley, "Effects of Nonlinear Reservoir Compaction on Casing Behavior," *SPE Prod. Eng.*, vol. 3, no. 03, pp. 333–338, 1988, doi: 10.2118/15469-pa.

[26] Y. P. Chia and D. A. Bradley, "Evaluation of Reservoir Compaction and Its Effects on Casing Behavior," *SPE Prod. Eng.*, vol. 4, no. 02, pp. 167–172, 1989, doi: 10.2118/15469-pa.

[27] A. Yudovich, L. V Chin, and D. R. Morgan, "Casing Deformation in Ekofisk," in *Proceedings*

of the Offshore Technology Conference, 1988, pp. 63–72, doi: OTC 5623.

[28] A. Klar, K. Soga, and M. Y. A. Ng, "Coupled deformation–flow analysis for methane hydrate extraction," *Géotechnique*, vol. 60, no. 10, pp. 765–776, 2010, doi: 10.1680/geot.9.P.079-3799.

[29] E. Xu, "Numerical Analysis of Wellbore Behaviour during Methane Gas Recovery from Hydrate Bearing Sediments," PhD thesis. University of Cambridge, 2014.

[30] T. Sasaki, K. Soga, and M. Abuhaikal, "Water absorption and shrinkage behaviour of early-age cement in wellbore annulus," *J. Pet. Sci. Eng.*, vol. 169, pp. 205–219, 2018, doi: 10.1016/j.petrol.2018.05.065.

[31] K. Yamamoto, "Overview and introduction: Pressure core-sampling and analyses in the 2012-2013 MH21 offshore test of gas production from methane hydrates in the eastern Nankai Trough," *Mar. Pet. Geol.*, vol. 66, pp. 296–309, 2015, doi: 10.1016/j.marpetgeo.2015.02.024.

[32] C. Teodoriu, Z. Yuan, J. Schubert, and M. Amani, "Experimental Measurements of Mechanical Parameters of Class G Cement," in *Proceedings of the SPE/EAGE European Unconventional Resources Conference and Exhibition*, 2012, pp. 1–7, [Online]. Available: https://doi.org/10.2118/153007-MS.

[33] K. Suzuki, T. Takayama, and T. Fujii, "Density structure report from logging-while-drilling data and core data at the first offshore gas production test site on Daini-Atsumi Knoll around eastern Nankai Trough," *Mar. Pet. Geol.*, vol. 66, pp. 388–395, 2015, doi: 10.1016/j.marpetgeo.2015.02.026.

[34] S. Nishio, E. Ogisako, and A. Denda, “Geotechnical Properties of Seabed Ground in East Nankai Trough,” in *Proceedings of the 7th International Conference on Gas Hydrates (ICGH 2011)*, 2011, pp. 1–4, [Online]. Available: https://doi.org/10.5026/jgeography.118.955.

[35] T. Sasaki, K. Soga, and M. Elshafie, “Simulation of wellbore construction in offshore unconsolidated methane hydrate-bearing formation,” *J. Nat. Gas Sci. Eng.*, vol. 60, pp. 312–326, 2018, doi: 10.1016/j.jngse.2018.10.019.

[36] A. Kumar, B. Maini, P.R. Bishnoi, M. Clarke, O. Zatsepina, and S. Srinivasan, “Experimental determination of permeability in the presence of hydrates and its effect on the dissociation characteristics of gas hydrates in porous media,” *J. Pet. Sci. Eng.*, vol. 70, pp. 114–122, 2010, doi: 10.1016/j.petrol.2009.10.005.

[37] J. Hou, Y. Ji, K. Zhou, Y. Liu, and B. Wei, “Effect of hydrate on permeability in porous media: Pore-scale micro-simulation,” *Int. J. Heat Mass Transf.*, vol. 126, pp. 416–424, 2018, doi: 10.1016/j.ijheatmasstransfer.2018.05.156.

[38] M. L. Delli and J. L. H. Grozic, “Experimental determination of permeability of porous media in the presence of gas hydrates,” *J. Pet. Sci. Eng.*, vol. 120, pp. 1–9, 2014, doi: 10.1016/j.petrol.2014.05.011.

[39] J. Sun *et al.*, “Numerical simulation on gas production from hydrate reservoir at the 1st offshore test site in the eastern Nankai Trough,” *J. Nat. Gas Sci. Eng.*, vol. 30, pp. 64–76, 2016, doi: 10.1016/j.jngse.2016.01.036.

[40] S. Uchida, “Numerical investigation of geomechanical behaviour of hydrate-bearing sediments,” PhD thesis. University of Cambridge, 2012.

[41] X. Sun, H. Luo, and K. Soga, “A coupled thermal–hydraulic–mechanical–chemical (THMC) model for methane hydrate bearing sediments using COMSOL Multiphysics,” *J. Zhejiang Univ. (Applied Phys. Eng.*, vol. 19, no. 8, pp. 600–623, 2018, [Online]. Available: https://doi.org/10.1631/jzus.a1700464.

[42] X. Sun, N. Nanchary, and K. K. Mohanty, “1-D modeling of hydrate depressurization in porous media,” *Transp. Porous Media*, vol. 58, no. 3, pp. 315–338, 2005, doi: 10.1007/s11242-004-1410-x.

[43] G. J. Moridis, M. B. Kowalsky, and K. Pruess, “TOUGH+HYDRATE v1.2 User’s Manual: A Code for the Simulation of System Behavior in Hydrate-Bearing Geologic Media,” 2012. doi: 10.1016/j.jcv.2004.05.021.

[44] A. Klar, S. Uchida, Z. Charas, and K. Yamamoto, “Thermo-hydro-mechanical Sand Production Model in Hydrate-bearing Sediments,” in *Proceedings of the International Workshop on Geomechanics and Energy – The Ground as Energy Source and Storage*, 2013, pp. 1–5, doi: 10.3997/2214-4609.20131988.

[45] S. Kimoto, F. Oka, T. Fushita, and M. Fujiwaki, “A chemo-thermo-mechanically coupled numerical simulation of the subsurface ground deformations due to methane hydrate dissociation,” *Comput. Geotech.*, vol. 34, no. 4, pp. 216–228, 2007, doi:

10.1016/j.compgeo.2007.02.006.

[46] M. Kakumoto, N. Tenma, Y. Sakamoto, K. Miyazakai, and K. Aoki, "Development of the Geo-mechanical simulation code COTHMA," in *Proceedings of the Ninth (2011) ISOPE Ocean Mining Symposium*, 2011, pp. 3–6, [Online]. Available: https://doi.org/10.1201/b17435-306.

[47] S. Gupta, C. Deusner, M. Haeckel, R. Helmig, and B. Wohlmuth, "Testing a thermo-chemo-hydro-geomechanical model for gas hydrate-bearing sediments using triaxial compression laboratory experiments," *Geochemistry, Geophys. Geosystems*, vol. 18, no. 9, pp. 3419–3437, 2017, doi: 10.1002/2017GC006901.

[48] X. Sun, H. Luo, T. Luo, Y. Song, and Y. Li, "Numerical study of gas production from marine hydrate formations considering soil compression and hydrate dissociation due to depressurization," *Mar. Pet. Geol.*, vol. 102, pp. 759–774, 2019, doi: 10.1016/j.marpetgeo.2019.01.035.

[49] S. Uchida, K. Soga, and K. Yamamoto, "Critical state soil constitutive model for methane hydrate soil," *J. Geophys. Res. Solid Earth*, vol. 117, no. B3, pp. 1–13, 2012, doi: 10.1029/2011JB008661.

[50] J. Yoneda *et al.*, "Mechanical properties of hydrate-bearing turbidite reservoir in the first gas production test site of the Eastern Nankai Trough," *Mar. Pet. Geol.*, vol. 66, pp. 471–486, 2015, doi: 10.1016/j.marpetgeo.2015.02.029.

[51] S. Nishio, E. Ogisako, and A. Denda, "Geotechnical Properties of Core Samples Recovered from

Seabed Ground in East Nankai Trough," *J. Geog.*, vol. 118, no. 5, pp. 955–968, 2009, [Online]. Available: https://doi.org/10.5026/jgeography.118.955.

[52] J. C. Santamarina *et al.*, "Hydro-bio-geomechanical properties of hydrate-bearing sediments from Nankai Trough," *Mar. Pet. Geol.*, vol. 66, pp. 434–450, 2015, doi: 10.1016/j.marpetgeo.2015.02.033.

[53] J. Yoneda *et al.*, "Consolidation and hardening behavior of hydrate-bearing pressure-core sediments recovered from the Krishna–Godavari Basin, offshore India," *Mar. Pet. Geol.*, vol. 108, no. September 2018, pp. 512–523, 2019, doi: 10.1016/j.marpetgeo.2018.09.021.

[54] J. Yoneda, M. Kakumoto, K. Miyazaki, J. Katagiri, K. Aoki, and N. Tenma, "Evaluation of Frictional Properties for Methane-Hydrate-Well Completion and Production," *SPE Drill. Complet.*, vol. 29, no. 01, pp. 115–124, 2014, [Online]. Available: https://doi.org/10.2118/169897-pa.

[55] T. Sasaki *et al.*, "Distributed fibre optic strain sensing of an axially deformed well model in the laboratory," *J. Nat. Gas Sci. Eng.*, 2019.

[56] M. Uesugi, H. Kishida, and Y. Uchikawa, "Friction between dry sand and concrete under monotonic and repeated loading," *Soil Sci. Soc. Am. J.*, vol. 30, no. 1, pp. 115–128, 1990, doi: 10.1248/cpb.37.3229.